

Florida State University Libraries

Electronic Theses, Treatises and Dissertations

The Graduate School

2010

Running over Unknown Rough Terrain with a One-Legged Planar Robot

Benjamin Andrews



THE FLORIDA STATE UNIVERSITY
COLLEGE OF ENGINEERING

RUNNING OVER UNKNOWN ROUGH TERRAIN WITH A ONE-LEGGED
PLANAR ROBOT

By
BEN ANDREWS

A Thesis submitted to the
Department of Mechanical Engineering
in partial fulfillment of the
requirements for the degree of
Master of Science

Degree Awarded:
Summer Semester, 2010

The members of the committee approve the thesis of Ben Andrews defended on June 07, 2010.

Jonathan Clark
Professor Directing Thesis

Emmanuel Collins
Committee Member

William Oates
Committee Member

Approved:

Chiang Shih, Chair, Department of Mechanical Engineering

Ching-Jen Chen, Dean, College of Engineering

The Graduate School has verified and approved the above-named committee members.

TABLE OF CONTENTS

List of Tables	v
List of Figures	vii
Abstract	xi
1 INTRODUCTION	1
1.1 Why Single Legged Robots?	1
1.2 History	1
1.3 Spring Loaded Inverted Pendulum Model of Legged Locomotion	2
1.3.1 Conservative SLIP template	2
1.4 Motivation	3
1.5 Summary of Motivating Control Ideas	3
1.6 Nominal Control Approaches	4
1.6.1 Fixed Impulse	4
1.6.2 Swing Leg Retraction	5
1.6.3 Active Energy Removal	6
1.7 Thesis Organization and Contributions	7
2 DESIGN	9
2.1 Platform Requirements	9
2.2 Mechanical Parameter Design	9
2.3 Experimental Structure	9
2.4 Mechanical Design and Manufacture	10
2.4.1 Initial Robot	11
2.4.2 Final Version	11
2.5 Computer and Electronic System	11
2.5.1 Hardware Components	11
2.5.2 Software Development	13
3 SIMULATION	21
3.1 Methods	21
3.1.1 Simulation Parameters and Tuning	21
3.2 Controller Modifications	23
3.2.1 Fixed Thrust	23
3.2.2 Actuated Swing Leg Retraction	23

3.2.3	Active Energy Removal	24
3.3	Choosing Optimal Controller Parameters	24
3.4	Simulation Results and Discussion	27
3.4.1	Comparison of Active Energy Removal $v1$ and $v2$ controllers	27
3.4.2	Comparison of Raibert Fixed Impulse and Fixed Thrust	28
3.4.3	Actuated Swing Leg Retraction	29
3.4.4	Simulation Conclusions	30
4	EXPERIMENTAL RESULTS	36
4.1	Motor Performance	36
4.2	Comparison of Simulated and Experimental Results	36
4.2.1	Active Energy Removal $v1$ (AER- $v1$) controller	37
4.2.2	Fixed Thrust controller	37
4.3	Controller Comparison	39
4.4	Summary of Experimental Results	39
5	CONCLUSIONS	47
5.1	Conclusions	47
5.2	Future Work	48
	Bibliography	49
	Biographical Sketch	51

LIST OF TABLES

2.1	Dynamically scaled parameters	10
3.1	Motor specifications. V_{rated} is the rated voltage of the motor, $V_{operating}$ is the operating voltage, ω_{noload} is the no-load speed, and τ_{stall} is the stall torque.	22
3.2	Simulation parameters.	23
3.3	Brute force optimal parameter search range for each controller. AER refers to the Active Energy Removal controller	26
3.4	The gait with the highest forward velocity was chosen from Fig 3.2 for the Active Energy Removal controllers $v1$ and $v2$. This table outlines key characteristics of that ‘optimal’ gait for both controllers.	29
4.1	Control parameters and simulation prediction of the three optimal gaits that were run on the physical system. AER-v1 is version 1 of the Active Energy Removal controller, while FT is the Fixed Thrust controller. Decay is the expected average decay ratio of apex height and forward velocity following a step perturbation.	37
4.2	Comparison of simulation and physical results for gait 1 of the Active Energy Removal $v1$ controller.	38
4.3	Comparison of simulation and physical results for gait 2 of the Active Energy Removal $v1$ controller.	38
4.4	Comparison of simulation and physical results for gait 3 of the Active Energy Removal $v1$ controller.	40
4.5	Comparison of simulation and physical results for gait 1 of the Fixed Thrust controller.	40
4.6	Comparison of simulation and physical results for gait 2 of the Fixed Thrust controller.	43

4.7	Comparison of simulation and physical results for gait 3 of the Fixed Thrust controller.	45
-----	--	----

LIST OF FIGURES

1.1	Stance and flight phases of the SLIP model	2
1.2	SLIP diagram of the Fixed Impulse controller	4
1.3	State diagram of the Fixed Impulse controller	5
1.4	SLIP diagram of the Swing Leg Retraction controller	6
1.5	State diagram of the Swing Leg Retraction controller	6
1.6	SLIP diagram of the Active Energy Removal controller	7
1.7	State diagram of the Active Energy Removal controller	8
2.1	Diagram of the robotic leg	14
2.2	A prototype version of the robot standing on the circular track. The boom goes to the pivot point in the center of the track, where the electronics can be seen.	15
2.3	A closeup of the prototype robot. The crank arm is shown in the vertical position. The crank motor can be seen just above the plastic hip that extends from the end of the boom.	16
2.4	Aluminum boom inserts replaced the plastic hip seen in Fig. 2.2 by allowing the hip motor to be embedded in the boom. These parts can be seen as blue and red discs in Fig 2.5.	17
2.5	CAD drawing closeup of the boom (translucent) and upper leg assembly. The hip motor can be seen located inside the boom, and the leg length actuation motor is attached at the top of the leg. The four-bar and lower leg assembly are not shown here.	17
2.6	A solid aluminum leg replaced the plastic prototype.	18
2.7	Final version of the robot complete on new boom assembly.	18

2.8	Complete electronic control system on perfboard. This system can be made much smaller by placing it on a PCB.	19
2.9	An overview of the electronic control system.	20
3.1	Center of mass height versus time over a drop-step perturbation	25
3.2	Simulation results showing the lowest average decay ratio (measure of stability) following both a drop step and raised step perturbation as a function of forward velocity. Diamonds indicate the decay ratios for the Active Energy Removal $v2$ controller, while ‘X’ marks the decay ratios for $v1$ of the controller. These gaits all have at least a $10.16cm$ apex height of the foot.	28
3.3	Simulation results showing the lowest average decay ratio (measure of stability) following both a drop step and raised step perturbation as a function of forward velocity. Squares indicate the decay ratios for the Fixed Thrust controller, while ‘+’ marks the decay ratios for the Fixed Impulse controller. These gaits all have at least a $10.16cm$ apex height of the foot.	30
3.4	Simulation results showing the lowest average decay ratio (measure of stability) following both a drop step and raised step perturbation as a function of forward velocity. Circles indicate the decay ratios for the Swing Leg Retraction control law, while triangles mark the decay ratios for the adaptive leg angle control law. These gaits all have at least a $10.16cm$ apex height of the foot.	31
3.5	Simulation results showing the lowest average decay ratio (measure of stability) following both a drop step and raised step perturbation as a function of forward velocity. Squares indicate the decay ratios for the Raibert Fixed Thrust controller, while ‘X’ marks the decay ratios for the Active Energy Removal controller. These gaits all have at least a $10.16cm$ apex height of the foot.	32
3.6	Stability as a function of velocity and amount of energy actively removed. Global color scheme: dark colors indicate low average decay ratio, while lighter colors denote a high average decay ratio. Forward velocity is the vertical axis, while the horizontal axis is the starting angle of the crank actuator. Zero indicates maximum active energy removal, while 1.57 correlates to not actively removing any energy. The white triangle marks the gait with the lowest average decay ratio. The title is in the following format: $Damping_{system}\% - [Decay_{min}, Decay_{max}]$. . .	34

3.7	Stability as a function of velocity and amount of energy actively removed. Local color scheme scaled for each subplot: dark colors indicate low average decay ratio, while lighter colors denote a high average decay ratio. Forward velocity is the vertical axis, while the horizontal axis is the starting angle of the crank actuator. Zero indicates maximum active energy removal, while 1.57 correlates to not actively removing any energy. The white triangle marks the gait with the lowest average decay ratio. The title is in the following format: $Damping_{system}\% - [Decay_{min}, Decay_{max}]$	35
4.1	Crank actuator angle during the course of one stride for the Fixed Thrust controller. Red line indicates the desired position, while the blue line is the actual position. The green circles represent touch-down events, and the red diamond is lift-off. At 0.046 seconds the assumed maximum compression event occurs (A). A fixed thrust to a crank angle of 100 deg is commanded, and the desired angle is achieved 15 ms before lift-off (B). At lift-off, the crank is commanded to 360 deg (C). After 150 ms the desired angle is reached (D), and the crank is ready for the next touch down.	39
4.2	Hip actuator angle during the course of one stride for the Fixed Thrust controller. Red line indicates the desired position, while the blue line is the actual position. The green circle represents the touch-down event, the red diamonds are lift-off events, and the black circle is apex. This shows the hip motor is able to position the leg to the correct angle just before apex.	41
4.3	COM height of robot (left) and simulation (right) before and after a drop step perturbation for gait 2 of the Active Energy Removal controller. Nominal leg length has been subtracted from COM height for illustration purposes.	42
4.4	Apex height of robot and simulation before and after a drop step perturbation for gait 2 of the Active Energy Removal controller.	42
4.5	Apex return map of robot and simulation before and after a drop step perturbation for gait 2 of the Active Energy Removal controller.	43
4.6	Apex height of robot and simulation before and after a raised step perturbation for gait 2 of the Fixed Thrust controller.	44
4.7	Apex return map of robot and simulation before and after a raised step perturbation for gait 2 of the Fixed Thrust controller.	44

4.8	Apex height of the Active Energy Removal $v1$ and Fixed Thrust controllers following a drop (left) and raised (right) step pertubation. Gait 1.	45
4.9	Average apex height of the Active Energy Removal $v1$ and Fixed Thrust controllers following a drop (left) and raised (right) step pertubation. Gait 2.	46

ABSTRACT

The ability to traverse over unknown, rough terrain is an advantage that legged locomotion has over wheeled systems. However, due to the complexity of multi-legged systems, researchers in legged robotics have not been able to reproduce the agility found in the animal kingdom. In an effort to reduce this complexity, researchers have developed single-legged models, or templates, to gain insight into the fundamental dynamics of legged running. Inspired by studies of animal locomotion, researchers have proposed numerous control strategies to achieve stable one-legged running over unknown, rough terrain. One such control strategy incorporates energy variations into the system during the stance phase by changing the force-free leg length as a sinusoidal function of time. In this research, a one legged planar robot capable of implementing this and other state-of-the-art control strategies was designed and built. Both simulated and experimental results are used to determine and compare the stability of the proposed controllers as the robot is subjected to unknown drop and raised step perturbations equal to 25% of the nominal leg length. This study illustrates the relative advantages of utilizing a minimal-sensing, active energy removal control scheme to stabilize running over rough terrain.

CHAPTER 1

INTRODUCTION

1.1 Why Single Legged Robots?

The ability of animals to adapt effortlessly to rough terrain has inspired roboticists in their quest to build legged machines capable of agile locomotion in a natural environment. As a first step towards the development and understanding of complex multi-legged systems, researchers have focused on single-legged hopping robots. By studying one-legged robots, it is possible to avoid complex leg coordination schemes and concentrate on developing controllers and systems that result in stable running [1]. In addition, recent work has shown that single-legged robots and models can help improve our understanding of the fundamental locomotion principles of multi-legged robots and animals, and has led to the design and control of 4 to 6 legged robotic systems capable of fast running in an outdoor environment. [1, 2, 3, 4].

1.2 History

The first single legged hopping robot was developed by Matsuoka, who wanted to model repetitive hopping in humans [5]. Matsuoka achieved “in place hopping” in a reduced gravity environment. In the following years, Marc Raibert and the MIT Leg Lab pioneered the study of running machines, leading to the development of both 2-dimensional and 3-dimensional one-legged hopping robots [6, 7]. Raibert utilized full state information to achieve stable running over known terrain; however, his systems utilized a pneumatic power system, which was not particularly efficient or suited for operation outside of the lab. In an effort to improve overall efficiency, Buehler and others employed low power DC motors in their robots and incorporated an energy efficient control strategy [8, 9].

Running models such as the Spring Loaded Inverted Pendulum (SLIP) were utilized to help researchers understand the fundamentals of legged locomotion [10]. While the equations of motion for these models are simple, they are capable of reproducing the center of mass (COM) motion and ground reaction force profiles created by the majority of running animals [11]. With the insight gained from studying ‘tem-

plates' such as the SLIP model, researchers began to create legged robots capable of stable gaits with minimal (if any) feedback [12].

1.3 Spring Loaded Inverted Pendulum Model of Legged Locomotion

A variety of reduced-order hopping models have been proposed, the most common of which is the conservative SLIP model. Due to its simplicity, numerous control approaches have been based upon this model.

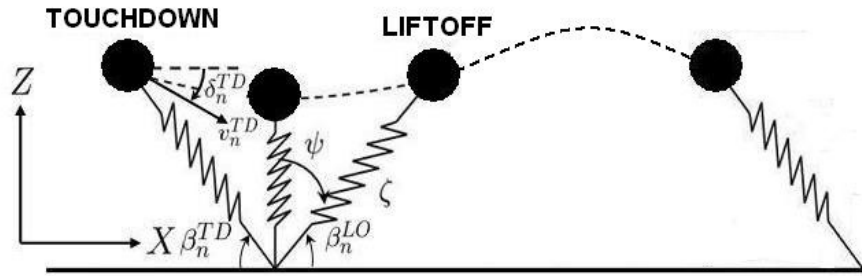


Figure 1.1: Stance and flight phases of the SLIP model

1.3.1 Conservative SLIP template

The body is modeled as a point mass m mounted on a massless leg of variable length ζ with an axially elastic, laterally rigid linear spring that has a spring constant k and a nominal length of l_o . The model is constrained to the sagittal plane, and each stride is decomposed into a stance phase and flight phase as depicted in Fig. 1.1. Stance begins at touch-down with velocity v_n^{TD} , and finalizes at lift-off when the force in the leg goes to zero. The elastic leg lifts off at an angle β_n^{LO} , continues with the flight phase, passes through the apex, and ends at touchdown: where a new stride starts. In Fig. 1.1, subscripts of the variables denote the stride number, while superscripts represent variables at touch-down (TD) or lift-off (LO).

The position of the center of mass during stance can be located in polar coordinates by (ζ, ψ) , and its evolution is determined using the following equations of motion [13]:

$$\begin{aligned}\ddot{\zeta} &= \zeta \dot{\psi}^2 - g \cos \psi - \frac{k}{m}(\zeta - l) \\ \zeta \ddot{\psi} &= -2\dot{\psi}\dot{\zeta} + g \sin \psi,\end{aligned}\tag{1.1}$$

where g represents gravity and $l = l_o$ for the nominal SLIP template.

The flight phase is modeled using simple ballistic dynamics:

$$\begin{aligned}\ddot{z} &= -g \\ \ddot{x} &= 0,\end{aligned}\tag{1.2}$$

where g is acceleration due to gravity.

1.4 Motivation

Previous research on hopping robots has focused mainly on flat terrain, terrain with known obstacles, and/or robots with numerous complex sensors and rigorous control algorithms. However, in order to further exploit the advantages of legged locomotion, it is necessary to be able to negotiate unknown, rough terrain. Studies of the *B. discoidalis* show that cockroaches and other insects rely largely on the intrinsic properties of their legs to recover from perturbations, rather than on neural feedback [14]. Additionally, drop-step perturbation studies performed on guinea fowl have demonstrated that stable locomotion can be maintained in animals when an unknown obstacle is encountered [15]. These studies have motivated researchers to create biomimetic robots with a reduced amount of sensors [16]. Reducing the number of sensors is advantageous because it allows the robot to weigh less, require less computation, consume less power, be more robust, and have less overall complexity. Furthermore, the excess computational power resulting from a minimal sensing system can be utilized for higher-level tasks such as navigation, path planning, and human-robot interaction. For these reasons, if autonomy is desired, minimal sensing becomes an attractive trait to complement the ability of traversing unknown, rough terrain.

1.5 Summary of Motivating Control Ideas

Fast recovery from ground induced perturbations is a key feature for any robotic system designed for efficient rough terrain traversal. This is particularly important if the robot is likely to encounter several severe changes in terrain height over the course of a few strides. Animals exploit several tactics to help recover from such perturbations. One insight gained from recent bio-mechanical studies is that animals' legs do not simply act like a spring, but that they actively dissipate, store, return, and produce energy throughout the stance phase [17, 18]. Following this idea, Schmitt presents simulation results of a lossless one-legged planar robot that achieves stable gaits over unknown, rough terrain by varying the force-free leg length and incorporating an adaptive control law for the leg touch down angle. However, as pointed out by the author, the system takes several hops to recover from a drop in terrain height [13]. Seyfarth et al. introduces an alternative control scheme which uses a swing leg retraction technique [19]. This method seems to result in faster recovery than the leg length actuation controller, when presented with similar perturbations. However, it is important to note that a system utilizing this form of Swing Leg Retraction converges to a different gait after being perturbed. Raibert proposed several

controllers for one-legged hopping robots [6]. However, these controllers require more state information than is easily sensed on a physical system. To circumvent this issue, a ‘minimal sensing’ version of one of Raibert’s controllers is proposed in this thesis.

1.6 Nominal Control Approaches

While many control strategies exist, three basic control approaches are considered for implementation on the physical system in this thesis. The first controller was chosen as a basis of comparison, or ‘control case’, due to its history in legged robot control. The second controller, ‘Swing Leg Retraction’, is a more modern control approach, and is used as a basis of comparison as well. The final controller, ‘Active Energy Removal’, has never been implemented on a physical system.

1.6.1 Fixed Impulse

Raibert and his colleagues at CMU and at the MIT Leg Lab pioneered the idea of decoupled control laws in running robots. To control these running robots, he designed controllers which utilized the following three control laws collectively: apex height, forward velocity, and body attitude. Raibert assumed that the controller laws could be designed and governed independently, even though the motions of the physical system were dynamically coupled.

The apex height control law added energy to the system by impulsing a fixed amount of energy into the system each stride, beginning at max leg compression. This constant amount of energy addition, controlled by a human operator via a potentiometer, resulted in a steady state hop height proportionate to the quantity of energy added.

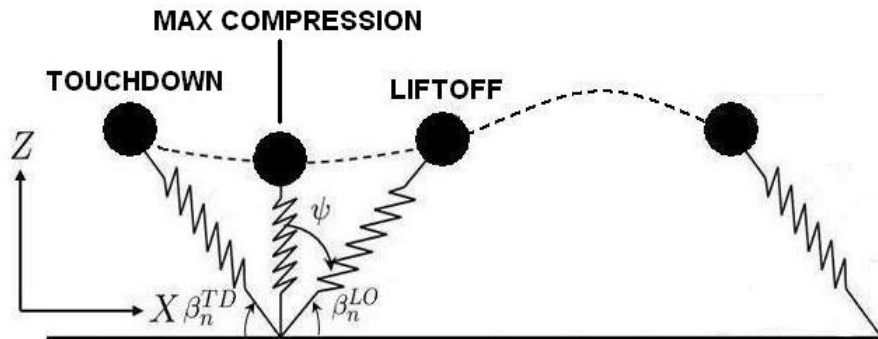


Figure 1.2: SLIP diagram of the Fixed Impulse controller

Forward velocity was controlled by utilizing a leg angle control law to calculate the touch-down angle of the leg. Raibert designed this leg angle control algorithm to

place the foot contact at the predicted midpoint of the upcoming stance. It is defined by:

$$\beta_{n+1}^{TD} = \arccos \left(\frac{\dot{x}T_s}{2l_0} + \frac{K(\dot{x} - V_{des})}{l_0} \right) \quad (1.3)$$

where \dot{x} is the forward velocity from the previous stance, T_s is the previous stance time., V_{des} is a parameter that influences forward velocity, K is a gain selected to maximize stability, and l_0 is the nominal leg length. [1].

The body attitude control law utilizes a gyroscope and hip torques to maintain the body in an upright position; however, this control law can be disregarded in this thesis, because the body attitude of the author's physical robot is held constant by a boom. This is also the case for 4 – 6 legged systems.

The Fixed Impulse controller is one of Raibert's early formulations, but it is one of the few controllers presented by him that can be adapted to a minimal sensing version. The sensing of three events (lift-off, touch-down, and maximum compression) is necessary for implementation of this controller, as shown in Figs. 1.2 and 1.3.

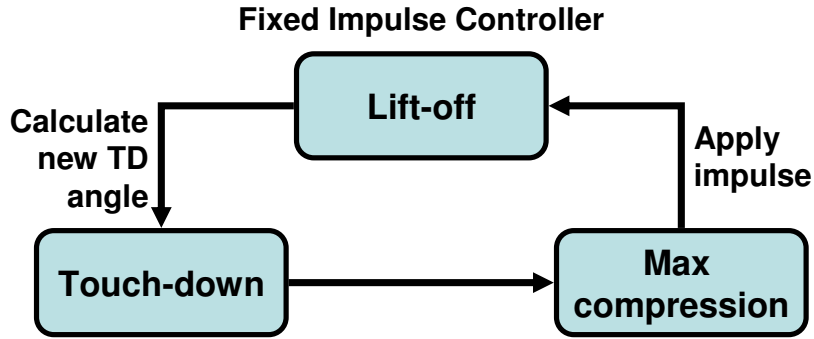


Figure 1.3: State diagram of the Fixed Impulse controller

1.6.2 Swing Leg Retraction

In the approach of [19], the swing leg is not held fixed during the flight phase, as depicted by Fig. 1.1, rather the swing leg varies its orientation $\alpha(t)$ as follows:

$$\alpha(t) = \begin{cases} \alpha_R & , t \leq t_{APEX} \\ \alpha_R + \omega_R(t - t_{APEX}) & , t > t_{APEX} \end{cases} \quad (1.4)$$

where α_R is the retraction angle (angle of the leg with respect to the ground at apex), ω_R is the constant angular speed of leg retraction, and t_{APEX} is the time at apex.

Since the Swing Leg Retraction model is conservative, the equations of motion during stance and flight are the same as the EOM for the nominal SLIP template Eq

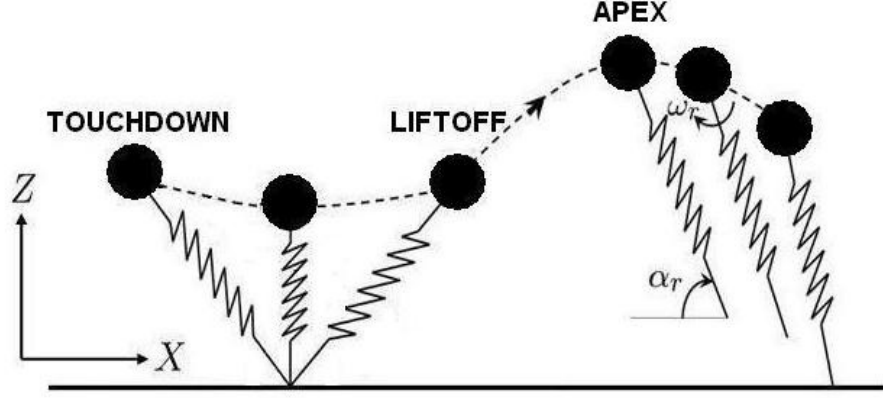


Figure 1.4: SLIP diagram of the Swing Leg Retraction controller

(1.1,1.2). In this paper, this controller will be referred to as the ‘Swing Leg Retraction’ controller. The sensing of three events (lift-off, touch-down, and apex) is necessary for implementation of this controller, as shown in Figs. 1.4 and 1.5.

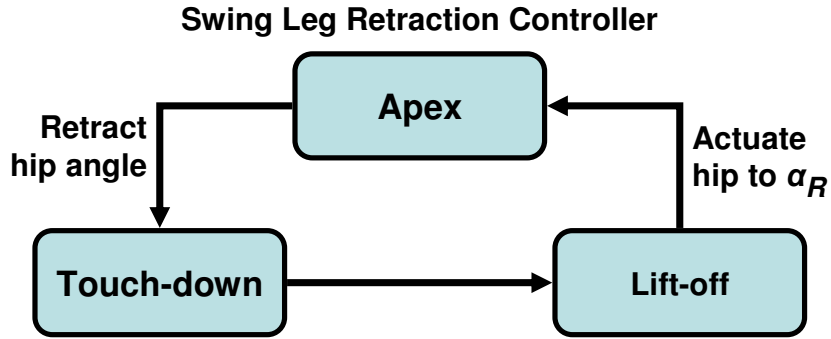


Figure 1.5: State diagram of the Swing Leg Retraction controller

1.6.3 Active Energy Removal

As mentioned previously, Schmitt introduced an energy modulation scheme, which operates by varying the force free leg length l as:

$$l = l_0 - l_{dev} \sin \frac{\pi t}{t_{des}}, \quad (1.5)$$

where l_0 represents the nominal leg length, l_{dev} is maximum deviation from the nominal leg length and t_{des} is a timing based mechanism for leg actuation [13]. It is

important to note that $t = 0$ at every touchdown. By varying the force-free length of the leg, potential energy is removed from the system during the first half of stance, and added during the second half. In the nominal case, the same amount of energy is added and removed from the system. However, in the presence of perturbations, the lift off event may occur early or late, which in turn determines the amount of energy added to the system. In summary, there are two novel ideas incorporated into this control law: it actively removes a fixed amount of energy from the system, and it adds an automatically varying amount of energy back into the system.

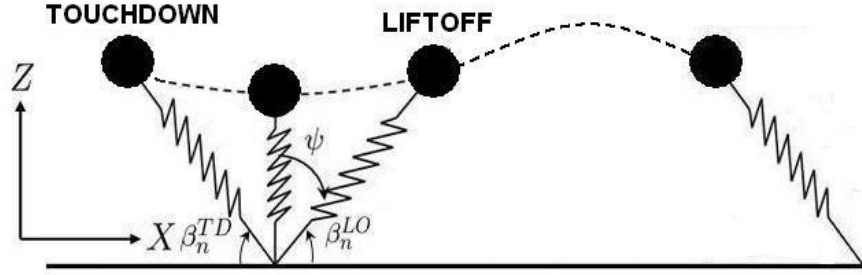


Figure 1.6: SLIP diagram of the Active Energy Removal controller

In addition to the energy modulation scheme given by (1.5), Schmitt proposed an adaptive leg touchdown angle control law to compensate for energy variations due to perturbations acting on the system. There are two different versions of this control law, as described in [13] and [20]. Version one of this control law is given by

$$\beta_{n+1}^{TD} = \beta_n^{LO} + c(\beta_n^{TD} - \beta_{des}^{TD}), \quad (1.6)$$

Version 2 of this control law adds an additional control parameter, and is described by:

$$\beta_{n+1}^{TD} = c_1 \beta_n^{TD} + c_2 \beta_n^{LO} + c_3 \beta_{des}^{TD}, \quad (1.7)$$

where β_n^{LO} , β_n^{TD} , and β_{des}^{TD} correspond to the previous lift-off angle, the previous touch-down angle, and the desired touch-down angle. The constants c , c_1 , and c_2 are control parameters, and $c_3 = 1 - c_2 - c_1$. For convenience, this controller will be referred to as the ‘Active Energy Removal’ controller. The sensing of two events (lift-off and touch-down) is necessary for implementation of this controller, as shown in Figs. 1.6 and 1.7.

1.7 Thesis Organization and Contributions

In this thesis, the stability of the control approaches introduced in Section 1.6 is compared and analyzed both in simulation and on a physical system. Chapter 2

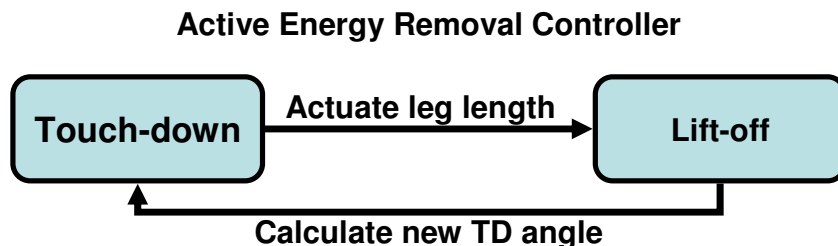


Figure 1.7: State diagram of the Active Energy Removal controller

describes the design and construction of a one legged hopping robot utilized to test the effectiveness of Active Energy Removal (and other) control strategies. A description of the simulation and results used to select appropriate control parameters is described in Chapter 3. Chapter 4 presents the experimental results from the physical system and compares those results to the simulation. Finally, Chapter 5 gives concluding remarks, including a discussion of future research.

Contributions of this thesis include the design, construction, simulation, and implementation of a robot capable of employing the Active Energy Removal controller as well as other competing controllers in the field. This thesis demonstrates the feasibility of the Active Energy Removal controller on a real-world system and compares its performance to both a classic control technique and a modern controller as well. Simulation and experimental results were used in an attempt to answer the following question: is active energy removal worth (from a stability perspective) the obvious loss in efficiency? Additionally, simulation results are presented in an effort to determine the relationship between inherent system damping and the optimal amount of energy to actively remove. These results suggest that while actively removing energy from the system increases stability regardless of system damping, it does so at a cost to velocity. The ‘optimal’ amount of energy to actively remove depends on the goals for that particular gait (is stability or high forward velocity a priority?).

CHAPTER 2

DESIGN

This chapter describes the mechanical design of the robot, electronics, and the experimental structure of the physical system.

2.1 Platform Requirements

In order to evaluate the effectiveness of the proposed leg control approaches, a robot with the following capabilities was required: sagittal plane motion and variation of nominal leg length as a sinusoidal function of time. The leg of the robot must be able to actuate to a specified angle with respect to the ground. The center of mass needs to be at or near the hip joint, and the robot should emulate a point mass. Additionally, the robot needs to be able to sense touch-down and lift-off events. This robot should be as similar to the SLIP model as possible, and maintain the physical characteristics of a 30% scale human runner. The smaller size was chosen for ease of physical implementation and testing.

2.2 Mechanical Parameter Design

Key values such as mass, spring stiffness, and leg length were obtained by dynamically scaling the values of a human runner. For reasons described in Section 2.1, a 30% scale was used. Proper dynamic scaling (as opposed to geometric scaling) results in the new system having scaled dynamic characteristics of the original system [21]. Additionally, if the system is dynamically scaled properly, the dynamic stability properties of the original system are preserved. The scaled parameters are shown in Table 2.1.

2.3 Experimental Structure

The robot is attached to a boom that pivots about a fixed point in the center of a circular track and can pivot up and down, as shown in Fig. 2.2. This effectively limits

Table 2.1: Dynamically scaled parameters

Quantity	Human Runner	30% Scaled
Mass	80 kg	2.16 kg
Stiffness	20000 N/m	1800 N/m
Leg Length	1 m	0.3 m

the robot to traveling in the sagittal plane. The initial track had a radius of 125cm, could be leveled with adjustable legs, and was comprised of 2" \times 4" lumber topped with 0.75" plywood. On top of the plywood was a 0.125" thick damped rubber mat, to prevent unwanted bouncing at touchdown and to increase traction. The original boom was a 2.54cm outer diameter aluminum tube with a wall thickness of 1mm. When the final version of the robot was built, the boom was upgraded as well. The new boom is still aluminum, and has a 5.715cm outer diameter and a wall thickness of 1mm. The larger diameter boom reduced flex, and allowed the hip motor to be inserted in the boom, eliminating the need for a separate hip.

Upon realization that the wooden track had undesirable variations in stiffness, the experimental platform was adjusted so that it could run on a carpeted floor. This new, uniform surface resulted in much smoother apex height and touch-down angle data.

2.4 Mechanical Design and Manufacture

To allow the variation of force free leg length, a crank slider mechanism was utilized. An electric DC motor at the top of the leg turns a crank of length l_{dev} , the crank is coupled to a linkage arm, and the linkage arm is joined to a linearly constrained slider, as shown in Fig. 2.1. This device converts a rotary actuator to a linear actuator, allowing the position of the slider, and therefore the force-free leg length, to be varied by rotating the motor shaft. Leg length l_0 is defined as the leg length when the slider, and consequently the leg length, is halfway between its shortest and longest positions.

At the bottom of the slider is a fixed linear bearing, with a movable 1/4" rod passing through it. The rod goes through the center of the leg spring (Century Spring part number 72067) and goes on to the foot, resulting in a 'coilover' spring configuration. The linear bearing allows the rod to travel smoothly, thus reducing losses when the spring compresses. The foot houses a simple plunger type switch, McMasterCarr part number 7658K17, which is used as a ground contact sensor.

The 'toe' is a aluminum hemisphere with a linear slide that attaches to the foot. The travel of the slide is limited to slightly less than the throw of the ground contact

sensor switch, which prevents the weight of the robot from being placed on the switch. The toe is what actually comes in contact with the ground during locomotion.

2.4.1 Initial Robot

The initial leg, hip, and foot were made using fuse deposition manufacturing (FDM), on a Stratus Dimension Elite 3d printer. The resulting ABS plastic parts were lighter than, although not as strong as, aluminum. Although still usable, the plastic parts were not very durable. The crank, linkage arm, and slider were made of aluminum. The 1/4" rod that passes through the spring was hardened steel. The initial robot can be seen in Figs. 2.2 and 2.3.

2.4.2 Final Version

A more robust version of the robot was built once the system was reliable and all adjustments were made. The final version of the robot is shown in Figs. 2.6 and 2.7. This involved making the leg out of solid aluminum, machined on a Haas MiniMill CNC. The hip was eliminated altogether by embedding the hip motor inside the boom via CNC milled aluminum inserts, as shown in Figs. 2.4 and 2.5. The 10.16cm long leg spring was replaced with a 15.24cm long spring to allow for more compression without bottoming out. There are lead weights attached to the boom to add mass; without the weights, the system is 750g lighter than it needs to be. The lead weights could possibly be replaced by batteries to make the system more autonomous.

2.5 Computer and Electronic System

An electronics control system was developed to meet the needs of the robot. The resulting system is roughly 32cm³ when placed on a PCB. It operates at 400MHz, and can easily control two motors in a PD loop at 2KHz while simultaneously storing state and 32 bit encoder position data. Each motor can draw up to 9A continuous, at up to 50V. The prototype circuit was developed on a breadboard, but when the final version of the robot was built, the electronics were more permanently mounted and soldered on a perfboard, as shown in Fig. 2.8. This allowed for a more robust circuit that was less prone to random errors caused by loose breadboard connections.

2.5.1 Hardware Components

The mainboard of the robot communicates with and controls the motor drivers, which control the motors. The encoders on the motors provide data to the decoder chip, and the decoder sends position data to the mainboard, as depicted in Fig. 2.9. All of the other sensors interface with the mainboard as well, and everything is governed by the control code.

Electronics. The control electronics consist of the mainboard, decoder chip, motor drivers, and an oscillator. The mainboard is a Gumstix Basix with a Breakout-gs board attached. The Basix is a mini computer $80mm \times 20mm$ that comes pre-installed with an embedded Linux operating system. It has a $400MHz$ Intel PXA255 processor with $64MB$ of RAM, expandable $16MB$ of memory, and Bluetooth wireless connectivity. With the attached Breakout-gs board, access is gained to 23 digital GPIO lines, I2C port, 5 serial UARTS, and 2 hardware based PWM lines.

The decoder chip is an Avago HCTL-2032 Quadrature Decoder. It has a 32-Bit counter, and can support two encoders. This chip decodes the data from the quadrature encoders, and the Gumstix mainboard receives the resulting position data in four individual bytes.

The motor driver used was the Pololu 36v9. The electronics system employed by the robot uses two of these motor drivers: one for each motor. Each motor driver is capable of up to $50V$, $9A$ continuous without a heat sink, and up to $12A$ continuous with a heat sink.

A $33MHz$ oscillator is used as a clock for the decoder chip. The oscillator is a *SG531PHC*, by Epson Toyocom Corporation.

Actuators. There are two actuators on the robot: the hip motor and the leg length actuation motor. The hip motor on the prototype was a Maxon Motor *RE25*, with a *GP32C* 28:1 reduction planetary gearhead. The leg length actuation motor was also a Maxon Motor *RE25* with a *GP32C*, but with a 5.8:1 reduction planetary gearhead. The final version of the robot used stronger motors, as the original Maxon motors failed (most likely due to axial loading caused from the drop step perturbations). The replacement motors are Faulhaber part number 3257 – 024CR, and have a 14 : 1 reduction planetary gearhead, series 32/3S.

The hip motor serves only to reset the hip angle during flight, and does no energy addition or removal to or from the system. The leg length actuation motor is the only actuator used to control system energy.

Sensors. The sensors can be divided into two categories: critical and auxiliary. The critical sensors are those required by the robot/controller to operate. Any given controller does not necessarily require all of the critical sensors listed. The auxiliary sensors are those that were added for safety during the development stage, or were added for additional data acquisition.

CRITICAL SENSORS. The ground contact sensor is required by all controllers. It detects the touch-down and lift-off events. A simple momentary plunger type switch was used to detect ground contact. When the switch is closed, the robot is in stance phase; when the switch is open, the robot is in flight phase. Switch debouncing is done in both software and hardware, and partially controlled by the lightly damped track surface. The software debouncing is done by latching the state of the switch for $50ms$. This means that once an event is detected, another event cannot be detected for a minimum of $50ms$. Hardware debouncing is achieved with a simple RC filter placed on the GPIO line of the switch.

Encoders on each of the motors provide important position data. The encoders are used to measure leg touch-down and lift-off angles, as well as nominal leg length. Both encoders are used for all controllers implemented.

AUXILIARY SENSORS. Encoders were placed on the boom to measure forward velocity and vertical height of the robot during operation. This data was collected by the Gumstix mainboard for off-line data analysis purposes only.

Safety cut-off switches were added for development purposes to detect when the leg angle was too large. These physical switches protected the robot from being damaged by turning off the motor drivers via a latching relay in the event that the hip motor actuated too far. The relays were also capable of being latched in software if the leg angle was too large or if the gumstix did not receive encoder data on the previous cycle.

2.5.2 Software Development

Gumstix is primarily developed in a Linux environment, although Microsoft Windows can be used as well. Practically any programming language that can be used in Linux can be used to program the Gumstix. C++ was chosen for all of the control code due to ease in implementation and the author's familiarity with the language.

Program Development. Gumstix uses the Open Embedded cross-compilation environment. With the Open Embedded environment, a program is developed and compiled on the host (development) machine. A program is developed as a "package," where a package consists of source code and a "recipe." A recipe is equivalent to a makefile; it simply tells the compiler how to compile the package. To compile the package, the command "bitbake" is used. Bitbake cross-compiles the package on the development machine in the machine language that is required for the Gumstix. The next step is to copy the compiled package from the development machine to the Gumstix and install it.

To access the gumstix, a ssh terminal is required. You can connect via usb-serial or bluetooth. Bluetooth was the preferred method due to the benefits of having a wireless connection. When the robot was finished with a run, data was transferred via bluetooth to the host machine and analyzed in Matlab.

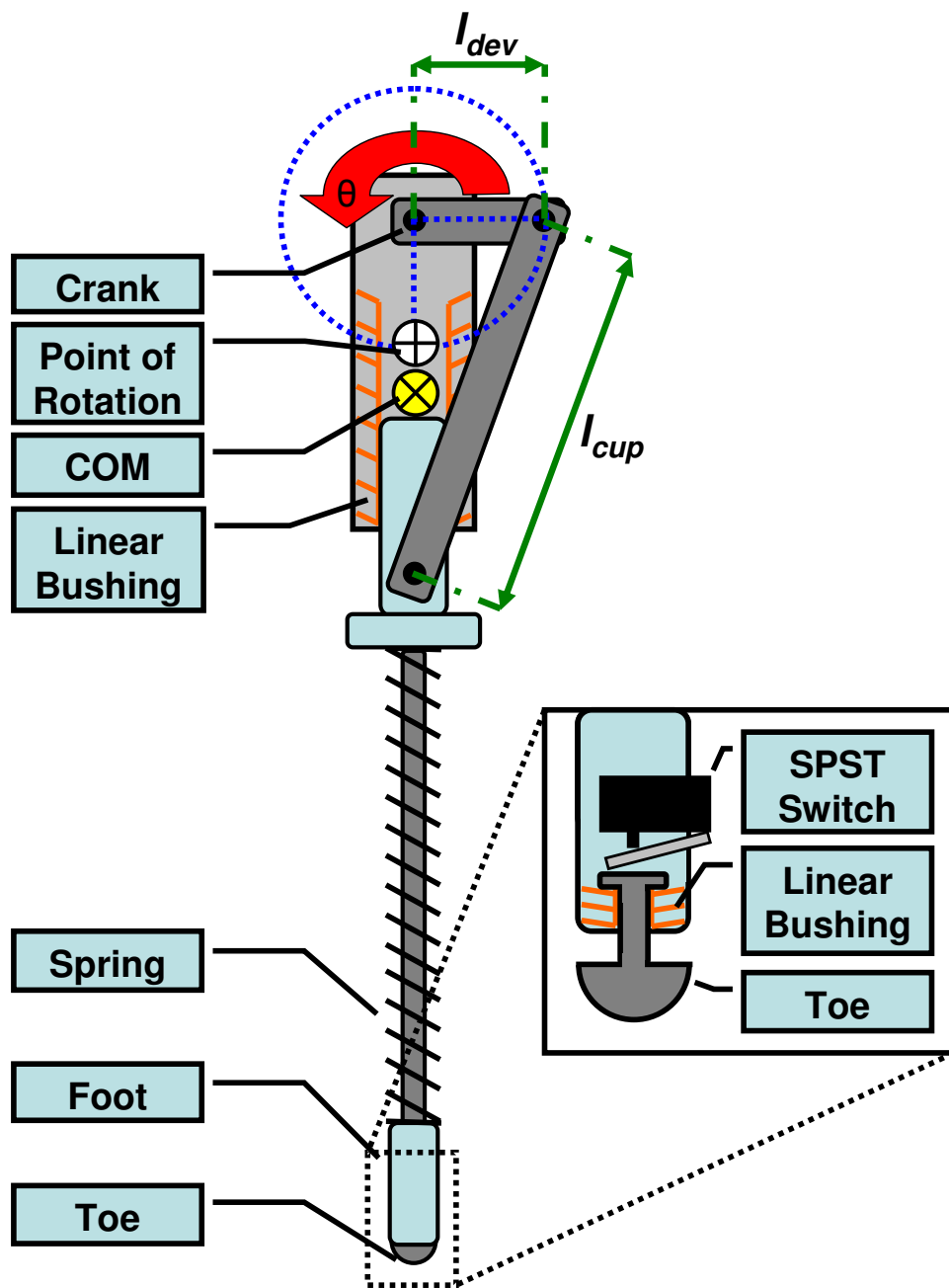


Figure 2.1: Diagram of the robotic leg

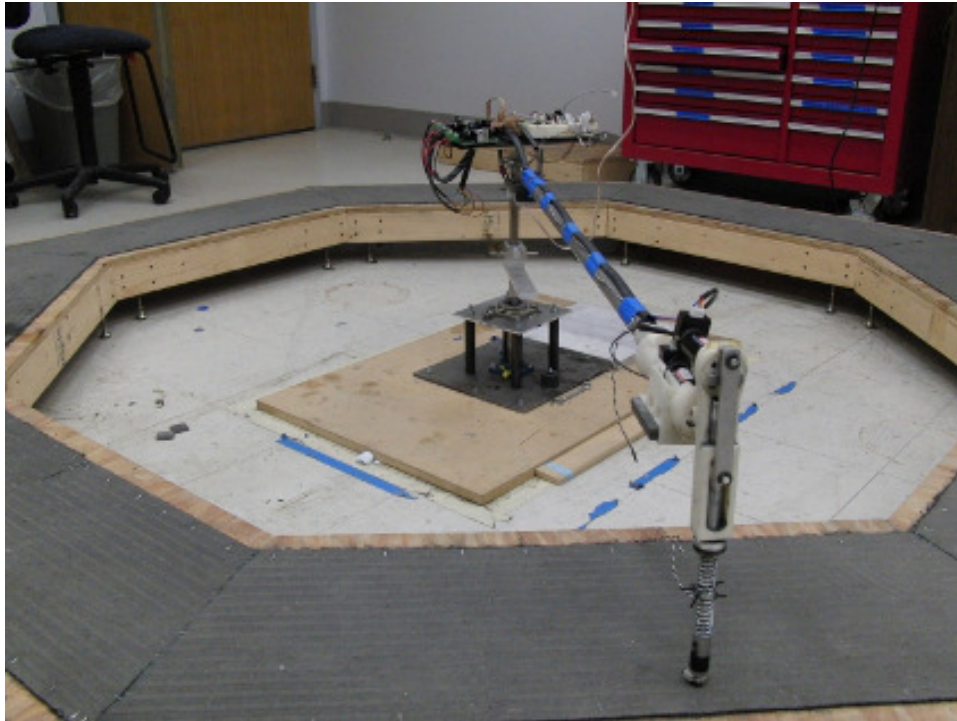


Figure 2.2: A prototype version of the robot standing on the circular track. The boom goes to the pivot point in the center of the track, where the electronics can be seen.

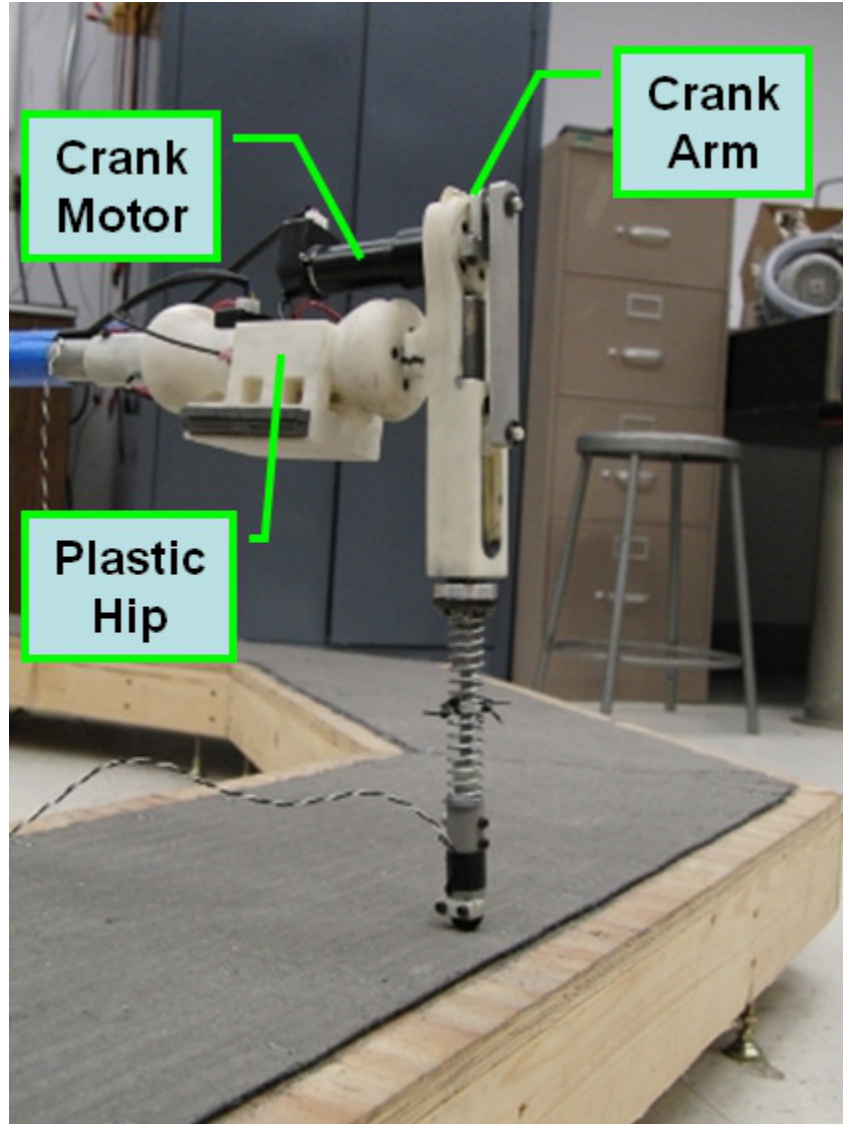


Figure 2.3: A closeup of the prototype robot. The crank arm is shown in the vertical position. The crank motor can be seen just above the plastic hip that extends from the end of the boom.



Figure 2.4: Aluminum boom inserts replaced the plastic hip seen in Fig. 2.2 by allowing the hip motor to be embedded in the boom. These parts can be seen as blue and red discs in Fig 2.5.

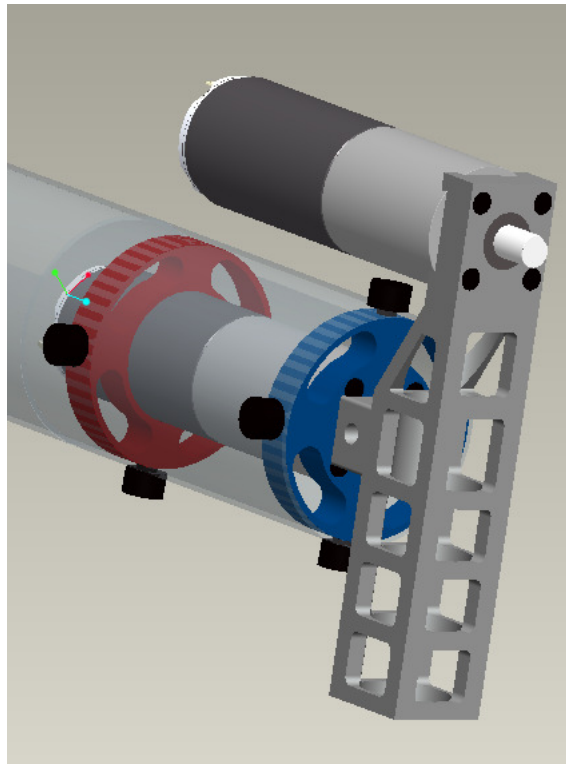


Figure 2.5: CAD drawing closeup of the boom (translucent) and upper leg assembly. The hip motor can be seen located inside the boom, and the leg length actuation motor is attached at the top of the leg. The four-bar and lower leg assembly are not shown here.

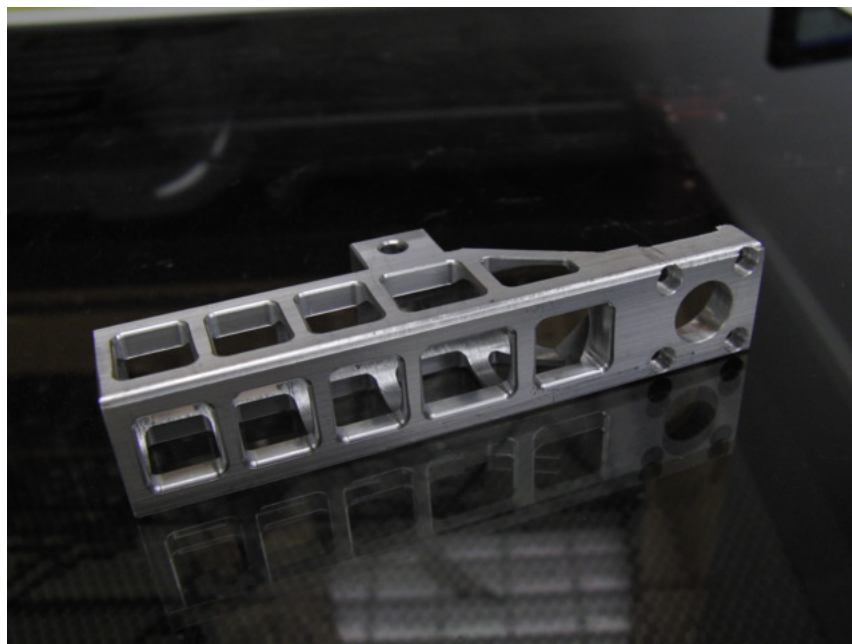


Figure 2.6: A solid aluminum leg replaced the plastic prototype.

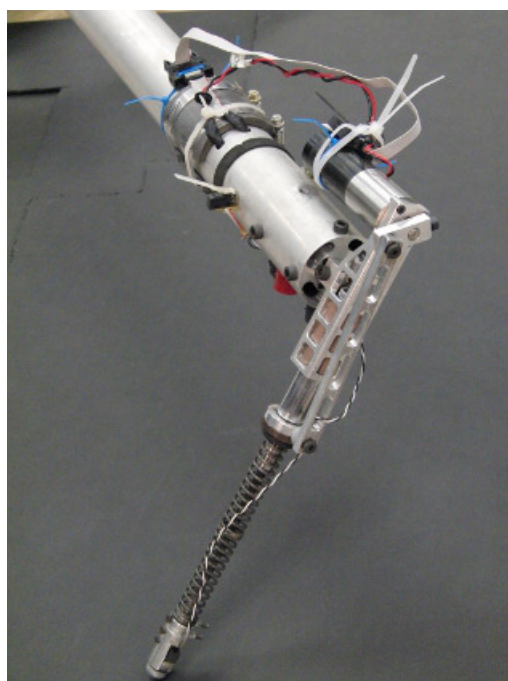


Figure 2.7: Final version of the robot complete on new boom assembly.

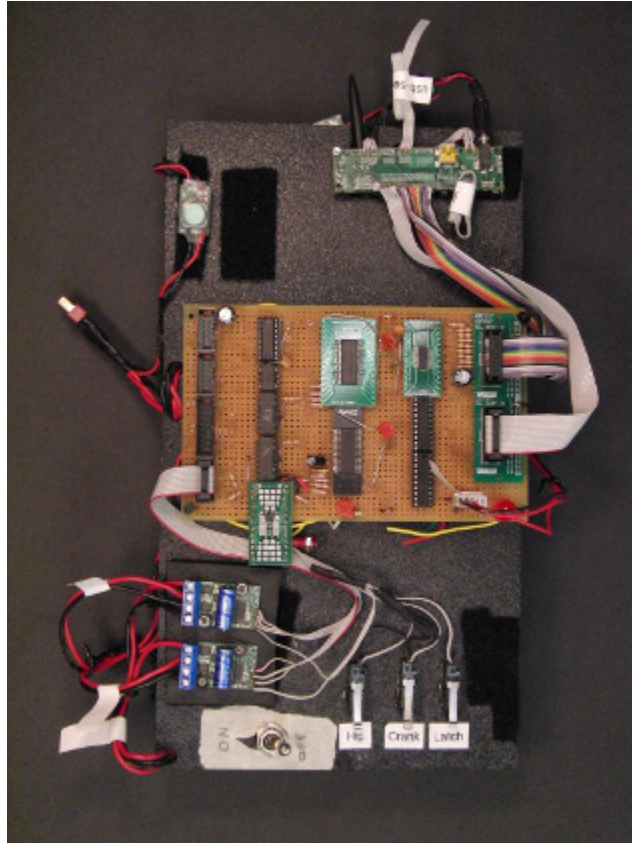


Figure 2.8: Complete electronic control system on perfboard. This system can be made much smaller by placing it on a PCB.

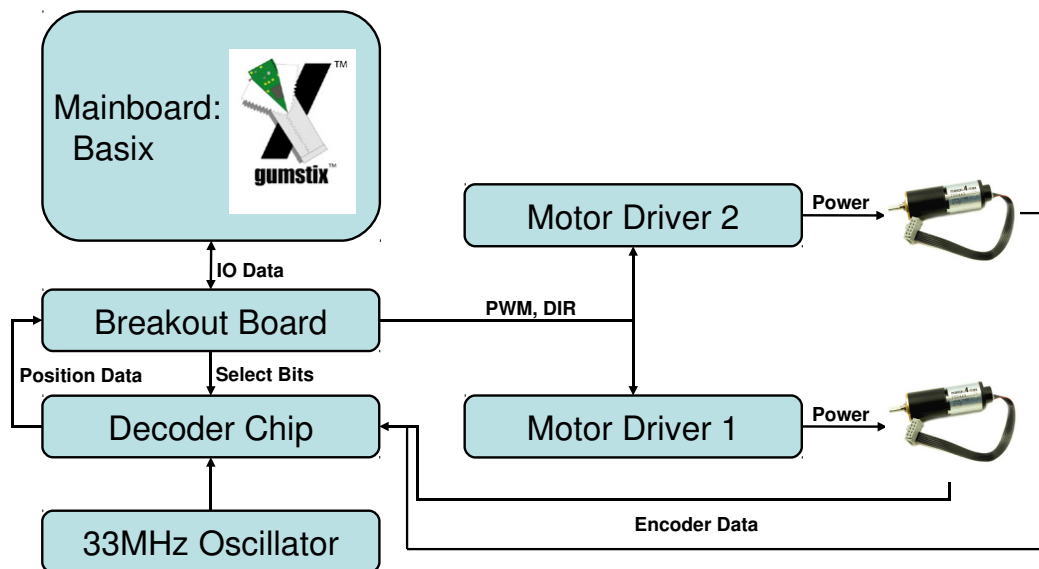


Figure 2.9: An overview of the electronic control system.

CHAPTER 3

SIMULATION

3.1 Methods

Numerical simulations of the controllers presented in Sec. 1.3 are performed using the Runge-Kutta integrator, *ode45*, from Matlab. Simulations are performed on terrain with both a drop step and a raised step perturbation equal to 25% of nominal leg length, and the locomotion performance is analyzed from a stability perspective. Both drop and raised step perturbations were chosen to simulate the effect of rough terrain that might be encountered outdoors.

The equations of motion used in the simulation are that of a non-conservative SLIP model during stance, described by:

$$\begin{aligned}\ddot{\zeta} &= \zeta \dot{\psi}^2 - g \cos \psi - \frac{k}{m}(\zeta - l) - \frac{\dot{\zeta}}{m} b_{linear} \\ \zeta \ddot{\psi} &= -2\dot{\psi} \zeta \dot{\zeta} + g \sin \psi - \frac{\dot{\psi}}{m} b_{rotational},\end{aligned}\tag{3.1}$$

where ζ is leg length, ψ is leg angle from vertical, l is force-free leg length, m is mass, b_{linear} is linear damping, and $b_{rotational}$ is the rotational damping of the hip joint.

During flight the simulation uses simple ballistic dynamics as shown in (1.2), and all losses due to air resistance are ignored.

3.1.1 Simulation Parameters and Tuning

The simulations were of a 30% scale human runner, and were modeled after the physical system. As discussed in Section 2.2, design points for basic physical properties of the robot were obtained through dynamic scaling. However, for an accurate simulation of the physical system, actual parameter values needed to be measured from the robot. These parameters can be found in Table 3.2.

Spring stiffness k was obtained by having the robot lock the leg perpendicular to the ground and hold the force free leg length at $l_0 - l_{dev}$. Next, a $6.8kg$ mass was added to the robot, and the leg length was measured. The spring stiffness was then calculated using Hooke's Law.

This leaves two ‘free’ parameters in the system: linear damping, b_{linear} , and rotational damping, $b_{rotational}$. A motor model and four-bar linkage device was implemented in the simulation to emulate the drive-train of the physical robot. This added an additional free parameter to the simulation, gear efficiency g_{eff} , that was able to account for losses in the drive mechanisms by scaling the speed-torque slope of the motor.

Values for the free parameters were chosen by recording data from four different gaits with two different controllers on the robot and comparing the results to the simulation. A comparison was made using six gait characteristics for each of the four gaits. The traits compared were the following: touch-down angle, lift-off angle, minimum stance height, apex height, forward velocity, and crank actuator angle at lift-off. A brute force search was then run in simulation to find the optimal values for b_{linear} , $b_{rotational}$, and g_{eff} . The optimal values were those that resulted in the least sum of the squares of the percent difference between the robot and simulation results.

To implement a motor model, the torque exerted on the crank motor by the four-bar linkage was calculated. This torque was then used to determine the maximum speed the crank motor could turn at that instant by utilizing the speed-torque slope of the motor. Table 3.1 shows the specifications for the motor and gear assembly used.

Table 3.1: Motor specifications. V_{rated} is the rated voltage of the motor, $V_{operating}$ is the operating voltage, ω_{noload} is the no-load speed, and τ_{stall} is the stall torque.

Motor Specification	Value	Unit
V_{rated}	24	V
$V_{operating}$	27.57	V
ω_{noload}	5900	rpm
τ_{stall}	0.539	N/m
Gear ratio	$\frac{676}{49}$	—

To more accurately represent the physical system, (1.5), the equation describing leg length actuation, was replaced with an equation incorporating the four-bar linkage:

$$l = l_{dev} \cos \theta + \sqrt{l_{cup}^2 - l_{dev}^2 \sin^2(\theta)} + l_C, \quad (3.2)$$

where l is the force-free leg length, l_{dev} is the maximum deviation from nominal leg length, θ is the angle made by the crank as calculated by utilizing the motor model and *ode45*, l_{cup} is the coupler length of the four-bar mechanism, and l_C is a constant defined by:

$$l_C = l_0 - l_{spring}, \quad (3.3)$$

where l_0 is the nominal leg length, and l_{spring} is the force-free length of the spring.

Table 3.2: Simulation parameters.

m	$2.113kg$
l_{dev}	$0.02m$
l_0	$0.298m$
l_C	$0.1544m$
l_{spring}	$0.1436m$
k	$1950N/m$
b_{spring}	$12.2Ns/m$
b_{hip}	$1.075Ns/m$
g_{eff}	0.45

3.2 Controller Modifications

Each of the controllers presented in Section 1.6 had to be modified in some way to accommodate the nonconservative nature of the physical system and/or the fact that the robot is minimal sensing. The following sections describe what adaptations were made to each controller.

3.2.1 Fixed Thrust

To enable implementation on the physical system, a minimal sensing version of the Fixed Impulse controller described in Section 1.6.1 is proposed. Due to the impracticality of administering an impulse, a ‘fixed thrust’ controller which extends the leg length as fast as possible to a constant desired length is instead utilized. The desired length will be a control parameter, θ_{des} , which will be a constant angle that the leg length actuation motor tries to obtain during stance.

A minimal sensing robot has no easy way to detect maximum compression and actual forward velocity. Therefore, for the leg angle control law, maximum compression is assumed to occur when the leg is perpendicular to the ground. Additionally, a forward velocity estimate is made by using the angle swept by the leg during stance and the stance time.

In summary, a minimal sensing version of the Fixed Impulse controller will be used. This controller exerts a fixed thrust by lengthening the leg during stance, starting when the leg is perpendicular to the ground.

3.2.2 Actuated Swing Leg Retraction

Swing-leg retraction was presented on a conservative model, and as such had no energy addition mechanism. To simulate this controller on the system presented in this paper, a form of actuation needed to be incorporated. This was done by utilizing the

four-bar mechanism already employed by the robot to extend the leg length during stance.

3.2.3 Active Energy Removal

The leg length actuation control law proposed by Schmitt calls for change in the force-free length of the spring. The physical system is not capable of doing that, but it does vary the force-free length of the leg, which should be equivalent.

3.3 Choosing Optimal Controller Parameters

Parameters for any given controller were considered ‘optimal’ when they resulted in a gait with the lowest average decay ratio of apex height and forward velocity over the course of four strides immediately following a perturbation. To determine the decay ratio for a given set a parameters, the simulation was run until both apex height and forward velocity were stable from stride to stride. Once this stability was achieved, a decrease in terrain height was introduced, and the apex of the next five hops as well as the forward velocity was recorded. This same procedure was repeated, only this time an increase in terrain height was introduced. The decay ratio of hop height for each apex was determined by,

$$decay_i = \left| \frac{apex_i - z_{ss}}{apex_{i-1} - z_{ss}} \right|, \quad (3.4)$$

where z_{ss} is the steady state apex height (adjusted for the step perturbation) and $apex_i$ is the apex height of the i^{th} hop since the step. The decay ratio was calculated for both apex height and forward velocity after both a drop step and the raised step perturbation, and then these four decay ratios were averaged to achieve the average decay ratio discussed from here on. Only gaits with an average decay ratio less than one were considered when choosing optimal gaits. An illustration of decay ratio calculation is shown in Fig. 3.1

The method of analyzing gait stability based on the average decay ratio of the first four hops following a perturbation was used as opposed to a more traditional approach of utilizing the eigenvalues of the linearized return map because the decay ratio can be measured on the physical system as well as in simulation, allowing a comparison to be made. Additionally, this stability metric was chosen based on the idea that in rough terrain, the first few hops after a large perturbation are most important. If a system encounters several ground induced perturbations over the course of a few strides, a gait capable of mostly recovering after a couple of strides is more desirable than a gait that recovers slowly, although completely, after many strides. Eigenvalues are a measure of the stability of a gait for small perturbations near steady state, whereas the average decay ratio is a indicator of the slope of the basin of attraction’s walls for large perturbations.

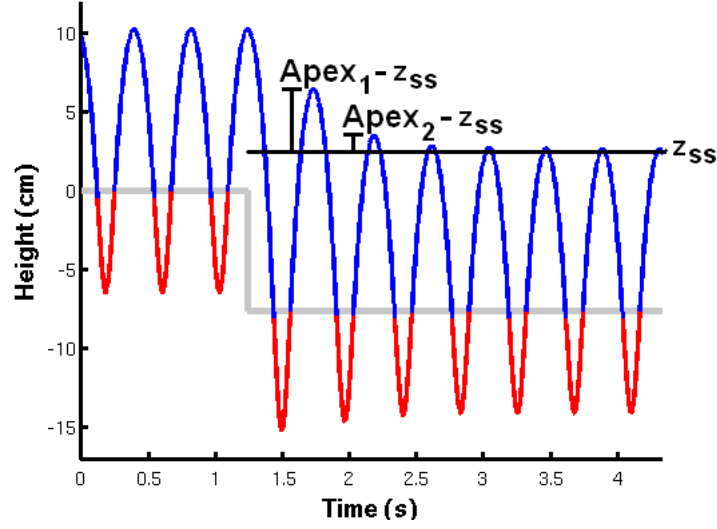


Figure 3.1: Center of mass height versus time over a drop-step perturbation

To find the optimal parameters for each controller, a brute force search was used. The Active Energy Removal *v1*, Fixed Impulse, Fixed Thrust, and Swing Leg Retraction controllers have a three-dimensional parameter space that is searched relatively quickly. Version 2 of the Active Energy Removal controller has a four-dimensional parameter space, but the viable parameters are small enough that the time required for a full search is reasonable. The ranges for the parameter space were chosen with multiple methods. The parameters c , $c1$, $c2$, K , and V_{des} were chosen by first searching a broad range at a coarse granularity. The results from the coarse search were used to determine reasonable values for the finer search. Parameters such as β_{des} , *Frequency*, θ_{des} , and α_r were chosen by physical limitations of the system, and/or the nature of the system. The range for β_{des} , the angle of the leg from horizontal, was chosen to be just shy of a fully vertical leg to a practically horizontal leg. Next, the minimum value for *Frequency* was chosen as the minimum motor speed required to make the physical system have a flight phase. The maximum value was chosen due to limitations of the crank motor. The range for θ_{des} was determined by the four-bar linkage itself. In order to only add energy (not actively remove any), the crank had to start in the vertical up position (π), and end no further than the vertical down position (2π). The range for α_r , the starting leg angle for Swing Leg Retraction, starts with the leg in the vertical position (minimum value) and goes to the leg in the fully horizontal forward position (maximum value). Finally, the range for ω_r was capable of being deduced by utilizing typical stance time and the range of α_r . The granularity (increment) used was chosen by trial and error. A summary of the parameters and the ranges searched can be found in Table 3.3.

A minimum steady state foot apex height (distance between the ground and the

Table 3.3: Brute force optimal parameter search range for each controller. AER refers to the Active Energy Removal controller

Controller	Parameter	Minimum Value	Maximum Value	Increment
AER-v1	β_{des}	0.8	1.4	0.015 <i>rad</i>
	c	0	1	0.025
	<i>Frequency</i>	4	6	0.05 <i>Hz</i>
AER-v2	β_{des}	0.8	1.4	0.015 <i>rad</i>
	$c1$	0	2	0.05
	$c2$	0	2	0.05
	<i>Frequency</i>	4	6	0.1 <i>Hz</i>
Fixed Impulse				
	K	0	0.03	0.0005
	θ_{des}	π	2π	$\frac{\pi}{45}$ <i>rad</i>
	V_{des}	3	40	0.25
Fixed Thrust				
	K	0	0.03	0.0005
	θ_{des}	π	2π	$\frac{\pi}{45}$ <i>rad</i>
	V_{des}	3	40	0.25
Swing Leg Retraction				
	α_r	0	$\pi/2$	0.015 <i>rad</i>
	ω_r	0	10	0.1 <i>rad/s</i>
	<i>Frequency</i>	4	6	0.05 <i>Hz</i>

foot) had to be enforced for the optimal gait search in order for the physical system to both be capable of resetting the leg angle during flight and have ample clearance of the step up in terrain height. Since the step height was 7.62cm , approximately 25% of the nominal leg length, the minimum apex height of the foot required for a gait was set to be 10.16cm .

3.4 Simulation Results and Discussion

This section presents the results from simulating the controllers, compares similar controllers, and ultimately discusses the selection of controllers to be implemented on the physical system. It should be noted that these control laws are not designed to explicitly control performance criteria such as hop height, speed, stability, efficiency, etc., but that these are emergent behaviors from a choice of control parameters. Although some controllers (in particular Fixed Impulse/Thrust) attempt to control individual performance metrics directly, these approaches are at best approximations due to the coupled dynamics of motion. More elaborate control laws could be developed to create a more direct mapping from control parameter to a particular performance criteria, but which performance criteria to choose remains an implementation specific question. Figs. 3.2, 3.3, 3.4, and 3.5 were created by first placing each gait found in the brute force parameter search in a velocity ‘bin’. A velocity bin contains a collection of gaits that fall into a specified velocity range, and there were 16 of these bins used between the minimum and maximum velocity found for each controller. Once the gaits were organized into bins, the gait with the lowest average decay ratio was found for each bin and plotted: resulting in the stability versus velocity graph. Each data point on these plots represents the ‘optimal’ gait for a particular controller, at a given range of velocity.

3.4.1 Comparison of Active Energy Removal $v1$ and $v2$ controllers

As shown in Fig. 3.2 and Table 3.4, the Active Energy Removal controllers $v1$ and $v2$ are functionally equivalent to each other. Fig. 3.2 shows that for any given velocity, the ‘optimal’ gate for both $v1$ and $v2$ of the AER controller result in very similar lowest average decay ratios. Table 3.4 highlights one gate from Fig. 3.2 and shows that the gait characteristics for both versions of the controller are similar as well. Since version 2 of the controller adds a fourth dimension to the control parameter space with no apparent benefit in stability or gait characteristics, only version 1 of the Active Energy Removal controller will be implemented on the physical system.

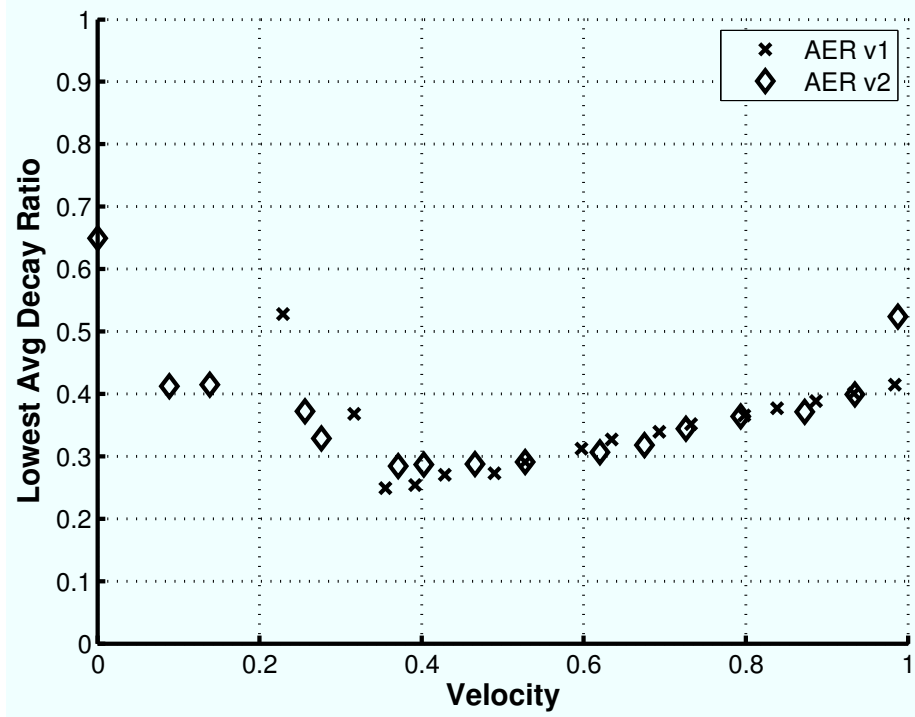


Figure 3.2: Simulation results showing the lowest average decay ratio (measure of stability) following both a drop step and raised step perturbation as a function of forward velocity. Diamonds indicate the decay ratios for the Active Energy Removal $v2$ controller, while ‘X’ marks the decay ratios for $v1$ of the controller. These gaits all have at least a $10.16cm$ apex height of the foot.

3.4.2 Comparison of Raibert Fixed Impulse and Fixed Thrust

While not quite equivalent, Fig. 3.3 shows the minimal sensing Fixed Thrust controller to have a stability trend similar to the Fixed Impulse controller proposed by Raibert. Although the Fixed Impulse controller is more stable at low velocities, the Fixed Thrust controller is both capable of higher velocities and is more stable at these higher velocities than the Fixed Impulse controller was at any velocity. Additionally, the robots the Fixed Impulse controller was originally implemented on were not capable of a true impulse, and as such, would likely have data points that fall somewhere between the simulated points shown in Fig. 3.3. For these reasons, the Fixed Thrust controller should be a fair basis of comparison to gauge the performance of the Active Energy Removal controller.

Table 3.4: The gait with the highest forward velocity was chosen from Fig 3.2 for the Active Energy Removal controllers $v1$ and $v2$. This table outlines key characteristics of that ‘optimal’ gait for both controllers.

Property	$v1$	$v2$	Units
Touch-down angle	9.74	9.78	deg
Lift-off angle	-15.26	-15.32	deg
Minimum stance height	-6.5	-6.5	cm
Apex height	10.2	10.2	cm
Stance time	0.132	0.132	s
Forward Velocity	0.98	0.99	m/s
Crank actuator angle at lift-off	262	262	deg

3.4.3 Actuated Swing Leg Retraction

Due to its nature, the Swing Leg Retraction controller has difficulties with raised step perturbations. This is because the hip angle is over-extended at apex and then begins to sweep in toward vertical. If a raised step perturbation is encountered, the leg will make contact with the ground at a larger ϕ (hip angle from vertical), thus slowing the system down more so than the step alone would have. This double loss of energy often results in the simulated robot falling backwards off of the step.

Swing Leg Retraction was simulated with various forms of leg length actuation: fixed thrust, active energy removal, and fixed velocity. Neither the fixed thrust nor the active energy removal methods of actuation combined with the Swing Leg Retraction control law resulted in gaits that met the stability criteria outlined in Section 3.3. Lastly, a fixed velocity method of actuation was simulated with Swing Leg Retraction, and stable gaits were found. The fixed velocity actuation extends the leg length at a constant rate, without actively removing any energy. As a basis of comparison, the Active Energy Removal controller was simulated with fixed velocity actuation as well. By doing this, a direct comparison can be made between the adaptive leg touch-down angle control law described by (1.6) and the Swing Leg Retraction control law.

As seen in Fig. 3.4, Swing Leg Retraction is capable of a narrower range of forward velocity. Furthermore, in the range of velocities that the two controllers overlap, the adaptive leg touch-down angle control law results in gaits that are more stable than Swing Leg Retraction. This supports the findings detailed by Schmitt and Clark in [20] concerning Swing Leg Retraction utilizing leg length actuation. In light of these results, and due to Swing Leg Retraction requiring an additional sensor, this controller will not be implemented on the physical system.

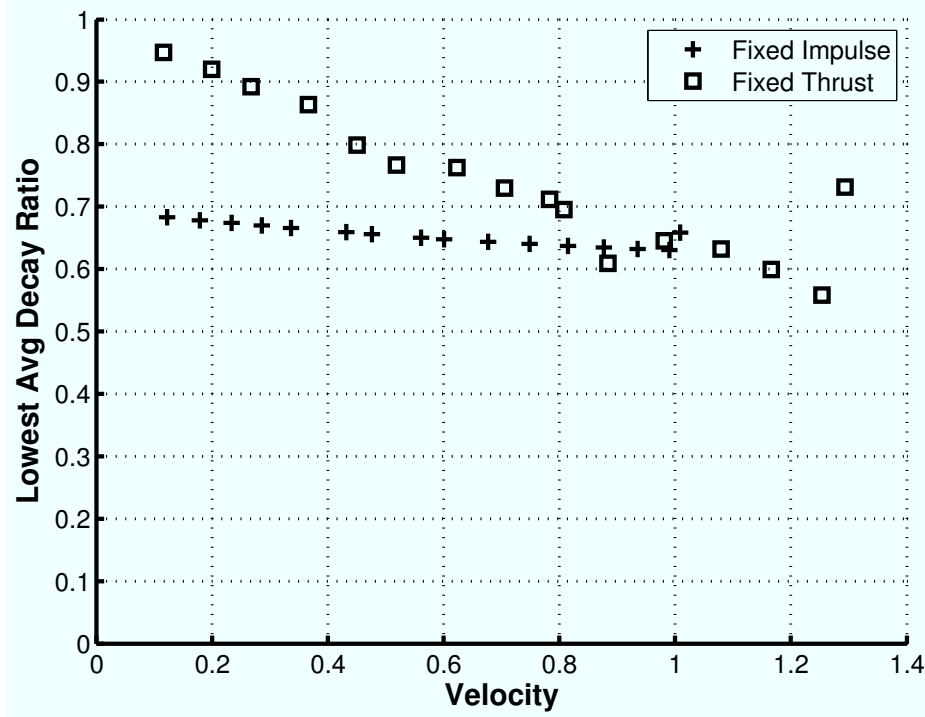


Figure 3.3: Simulation results showing the lowest average decay ratio (measure of stability) following both a drop step and raised step perturbation as a function of forward velocity. Squares indicate the decay ratios for the Fixed Thrust controller, while ‘+’ marks the decay ratios for the Fixed Impulse controller. These gaits all have at least a 10.16cm apex height of the foot.

3.4.4 Simulation Conclusions

Section 3.4.1 showed the near equivalence of $v1$ and $v2$ of the Active Energy Removal controller, while Section 3.4.2 suggested that the minimal sensing Fixed Thrust controller was a fair substitution for the Fixed Impulse controller. Finally, Section 3.4.3 concluded that Swing Leg Retraction offers no advantage over the adaptive leg angle control law in terms of stability, despite requiring the addition of an apex sensor. Considering these results, only the Active Energy Removal $v1$ controller and the Fixed Thrust controller was chosen to be implemented on the physical system. As shown in Fig. 3.5, the simulation results suggest the Active Energy Removal $v1$ controller is more stable than the Fixed Thrust controller at low velocities, but at higher velocities the stability of the two controllers begin to become more similar.

After observing Fig. 3.4, it is clear that at higher forward velocities, the system does not need to actively remove energy to maintain good stability. This makes sense because the dampers in the system are a function of velocity: the faster the mechanisms are moving, the more energy they will remove. With this information, the idea of a hybrid controller arises. Perhaps a controller utilizing the adaptive leg

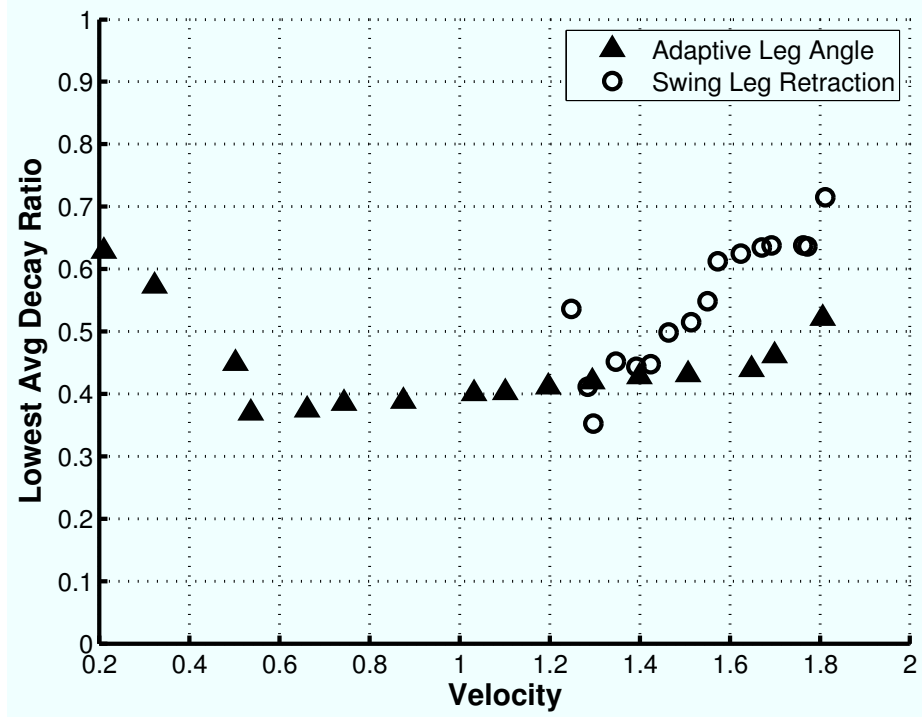


Figure 3.4: Simulation results showing the lowest average decay ratio (measure of stability) following both a drop step and raised step perturbation as a function of forward velocity. Circles indicate the decay ratios for the Swing Leg Retraction control law, while triangles mark the decay ratios for the adaptive leg angle control law. These gaits all have at least a 10.16cm apex height of the foot.

angle control law that actively removes energy up to a forward velocity of $1\frac{m}{s}$ as per the ‘X’s in Fig. 3.5, then switches to actively removing zero energy for faster gaits, like the high velocity gaits indicated by triangles in Fig. 3.4. However, the detailed development or characterization of a hybrid controller is beyond the scope of this thesis.

The prospect of a hybrid controller inspired an analysis of stability as a function of system damping, velocity, and the amount of energy actively removed from the system. Each subplot in Figs. 3.6 and 3.7, shows the ‘optimal’ gaits for a system with $x\%$ of system damping, where 100% equals the amount of damping in the experimental system discussed in Ch. 2. The stable gaits were divided into forward velocity bins (vertical axis), and the minimum average decay ratio for each bin is color mapped, with black being the lowest (best), the lightest shade being the highest, and a full spectrum in between. All average decay ratio values plotted are between zero and one. The horizontal axis is the crank actuator starting position, and corresponds to the amount of energy actively removed. Zero on the horizontal axis is the normal starting position for the Active Energy Removal controller, and corresponds to the maximum

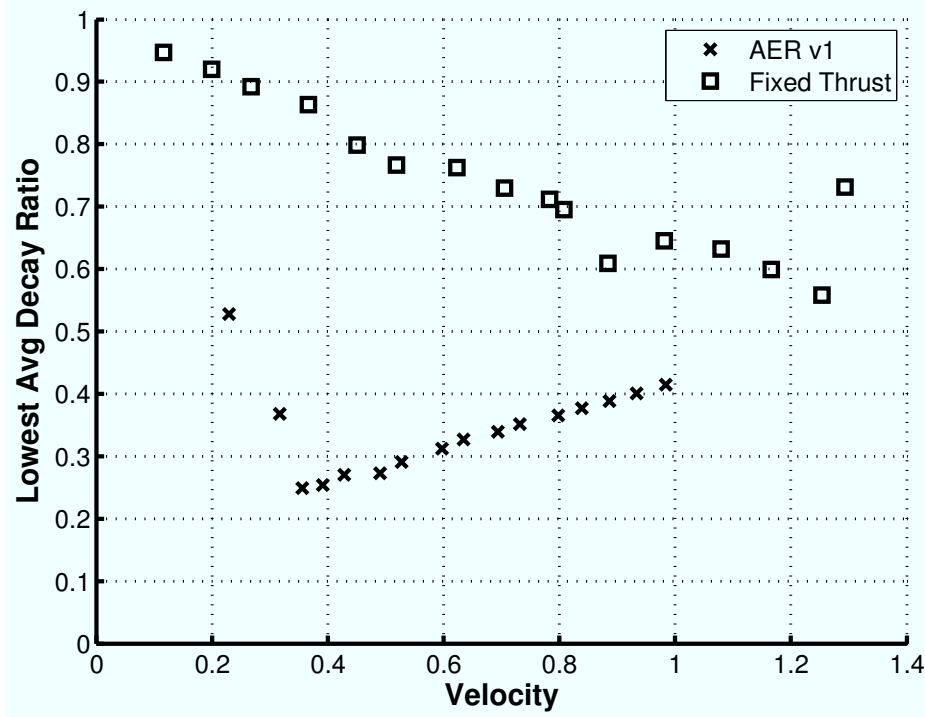


Figure 3.5: Simulation results showing the lowest average decay ratio (measure of stability) following both a drop step and raised step perturbation as a function of forward velocity. Squares indicate the decay ratios for the Raibert Fixed Thrust controller, while ‘X’ marks the decay ratios for the Active Energy Removal controller. These gaits all have at least a 10.16cm apex height of the foot.

amount of energy removed. The rightmost value on the horizontal axis is zero energy actively removed. This is the same as ‘fixed velocity’ actuation, as discussed in 3.4.3. The only difference between Fig. 3.6 and Fig 3.7 is the color scheme. The former has a ‘global’ color mapping: the minimum average decay ratio over *all* of the subplots is black, while the maximum is light copper shade. The latter figure has a ‘local’ color mapping, where each subplot gets its own full color spectrum.

Fig. 3.6 suggests the fastest gaits are those with system damping between 10–60%, while the most stable gaits occur when system damping is between 90 – 150%. It also shows that as system damping increases, maximum obtainable forward velocity decreases and stability increases. The white triangles indicate that the most stable gait on this system is a gait with maximum active energy removal: regardless of system damping.

Fig. 3.7 implies that while the most stable gait actively removes the maximum amount of energy, that gait is not much more stable (in some cases) than gaits that have a higher forward velocity as a result of actively removing zero energy. For example, when system damping is 120%, the highest forward velocity with maximum

active energy removal is 0.9m/s, with a average decay ratio of 0.3. However, with zero active energy removal, the highest forward velocity is 1.5m/s, with a average decay ratio of 0.5. This suggests that active energy removal is not always desirable (if a high forward velocity is more important than maximum stability), and that a trade-off between stability and speed exists.

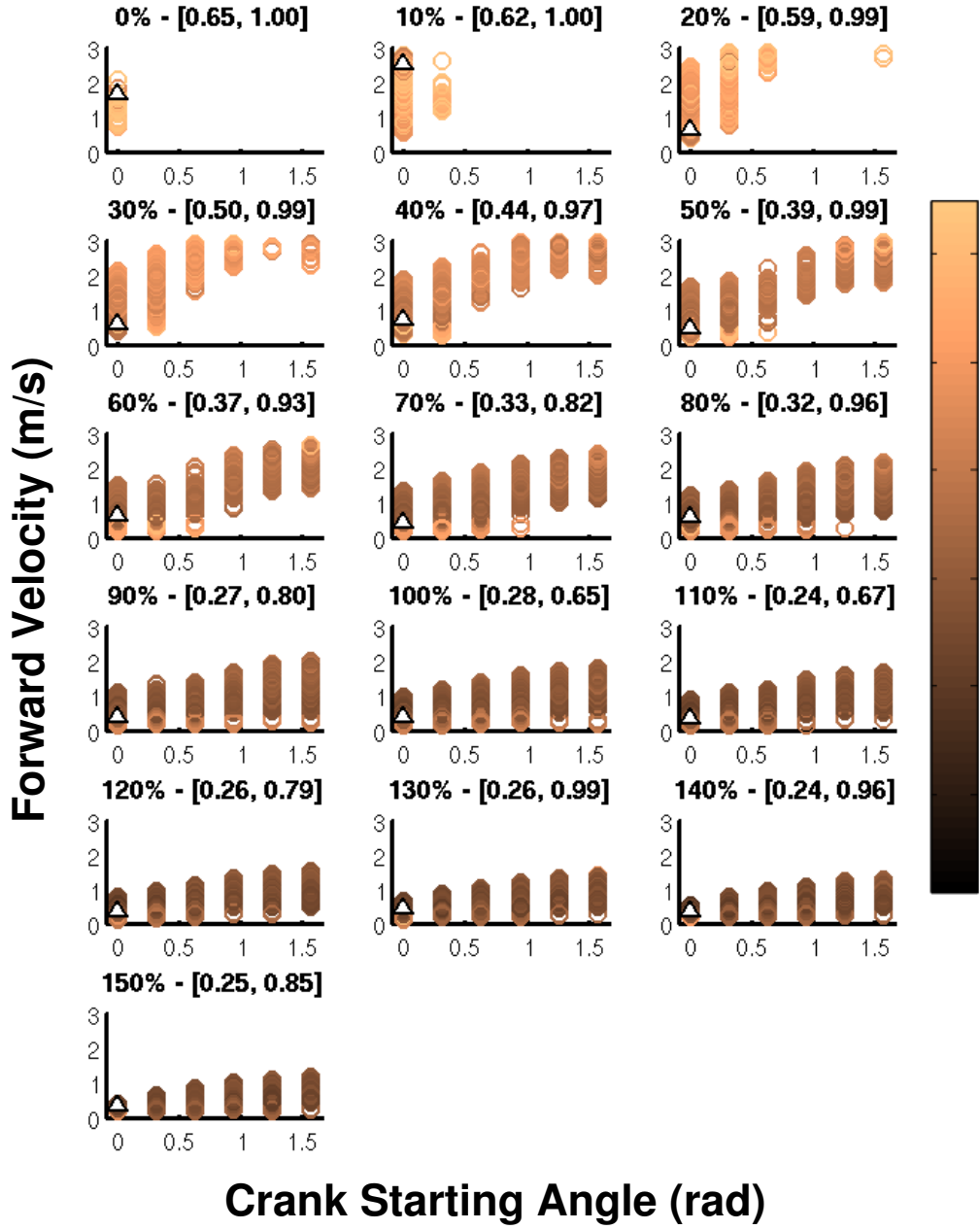


Figure 3.6: Stability as a function of velocity and amount of energy actively removed. Global color scheme: dark colors indicate low average decay ratio, while lighter colors denote a high average decay ratio. Forward velocity is the vertical axis, while the horizontal axis is the starting angle of the crank actuator. Zero indicates maximum active energy removal, while 1.57 correlates to not actively removing any energy. The white triangle marks the gait with the lowest average decay ratio. The title is in the following format: $Damping_{system}\% - [Decay_{min}, Decay_{max}]$

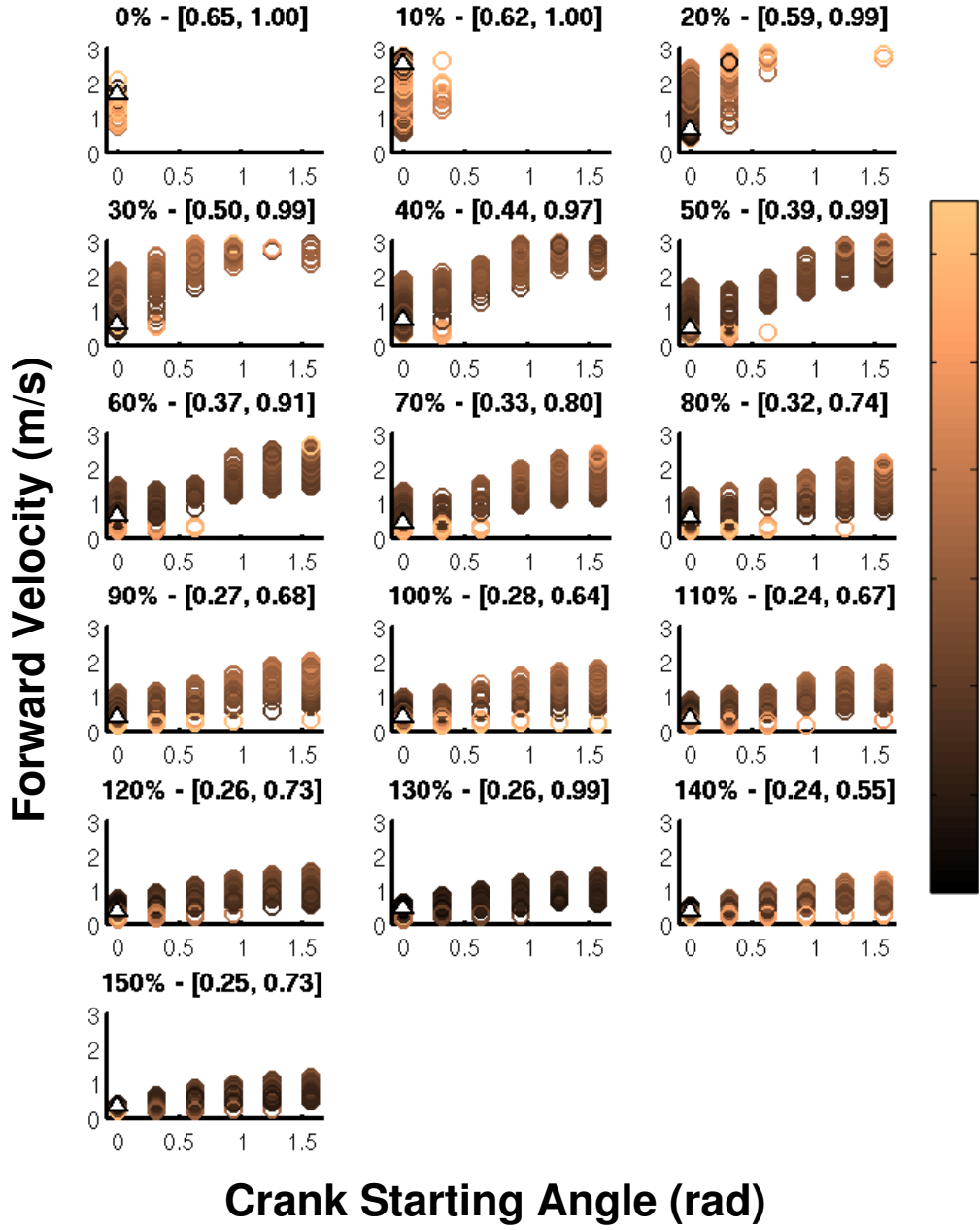


Figure 3.7: Stability as a function of velocity and amount of energy actively removed. Local color scheme scaled for each subplot: dark colors indicate low average decay ratio, while lighter colors denote a high average decay ratio. Forward velocity is the vertical axis, while the horizontal axis is the starting angle of the crank actuator. Zero indicates maximum active energy removal, while 1.57 correlates to not actively removing any energy. The white triangle marks the gait with the lowest average decay ratio. The title is in the following format: $Damping_{system}\% - [Decay_{min}, Decay_{max}]$

CHAPTER 4

EXPERIMENTAL RESULTS

For reasons discussed in Sec. 3.4, only the Schmitt *v1* and Raibert Fixed Thrust controller were implemented on the physical robot. Three points were chosen from Fig. 3.5 for each controller: a low, medium, and high velocity gait. Each of these gaits was run on the robot, and the results compared to the predictions of the simulation. Details of the gaits chosen can be found in Table 4.1.

4.1 Motor Performance

The DC motors were able to track the desired positions well utilizing a proportional-derivative feedback control law. The PD loop operates at $2KHz$, and the gains were chosen through physical experimentation. Figs. 4.1 and 4.2 show the desired and actual positions of the two motors during a stride. It should be noted that Fig. 4.1 begins at touch-down, while Fig. 4.2 begins at lift-off.

4.2 Comparison of Simulated and Experimental Results

This section compares the experimental results with the predictions of the simulation for both controllers undergoing both drop and raised step perturbations. There are three types of figures shown here: center of mass height versus time, apex height versus stride number, and an apex height return map. The first type is self explanatory, while the second simply shows the foot height at apex. A stride number of negative one or zero indicate hops before the perturbation was encountered, whereas a stride number of one or greater designates recovery hops after the step perturbation. An apex return map is simply the apex height of the current stride plotted against the apex of the next stride. In steady state, the apex height would be the same from stride to stride, resulting in a data point that falls on a 45° line in the return map. The 45° line represents stable locomotion, and as such, a stable system will always eventually return to that line. Due to the height change of the step perturbation,

Table 4.1: Control parameters and simulation prediction of the three optimal gaits that were run on the physical system. AER-v1 is version 1 of the Active Energy Removal controller, while FT is the Fixed Thrust controller. Decay is the expected average decay ratio of apex height and forward velocity following a step perturbation.

AER-v1	c	$\beta_{des}(rad)$	$Frequency(Hz)$	Apex (cm)	Velocity (m/s)	Decay
gait 1	0.400	1.40	4.85	10.3	0.3556	0.2487
gait 2	0.425	1.28	5.45	11.5	0.6936	0.3396
gait 3	0.400	1.16	6.00	10.2	0.9841	0.4149
FT	K	$\theta_{des}(rad)$	V_{des}	Apex (cm)	Velocity (m/s)	Decay
gait 1	0.0095	4.695	3.00	11.0	0.3670	0.8638
gait 2	0.0180	4.904	4.75	11.3	0.8080	0.6950
gait 3	0.0150	5.393	8.25	10.4	1.2536	0.5582

the trajectory must proceed from one point on the steady-state (45°) line to another point. The speed, or slope of the return trajectory is an indication of the stability of the gait. On the return map figures, the dashed line is the 45° line, the colored lines are the robot data, and the black line is the average of the robot data. Each segment is representative of one stride. The return maps start with a blue color, and work through the spectrum toward red.

4.2.1 Active Energy Removal v1 (AER-v1) controller

The simulation predicted the robot’s behavior fairly well on the three ‘optimal’ gaits tested. However, the robot did exhibit some period-2 tendencies that were not present in the model. Also, the steady state apex height of the robot on the step does not agree with the steady state apex height off the step. This is believed to be the result of the track and steps being comprised of different materials and topped with different surfaces. Regardless, the averaged physical data has a strong correspondence to the simulation, as shown in Figs. 4.3, 4.4, 4.5 and Tables 4.2, 4.3, 4.4.

4.2.2 Fixed Thrust controller

As illustrated in Figs. 4.6, 4.7 and Tables 4.5, 4.6, 4.7, the simulation predicted the robot’s behavior accurately on the three ‘optimal’ gaits tested. As with the Active Energy Removal controller, the steady state apex height of the robot on the step does not agree with the steady state apex height off the step. Again, this is believed to be the result of the track and steps being comprised of different materials and topped with different surfaces. However, the apex height still seems to fit the same decay

Table 4.2: Comparison of simulation and physical results for gait 1 of the Active Energy Removal *v1* controller.

Property	Simulation	Robot AVG	Robot STD	Units
Touch-down angle	4.47	4.80	1.19	deg
Lift-off angle	-7.28	-7.44	1.34	deg
Minimum stance height	-6.4	-6.0	0.6	cm
Apex height	10.7	8.5	0.7	cm
Stance time	0.143	0.151	0.003	s
Forward velocity	0.43	0.43	0.05	m/s
Crank actuator angle at lift-off	249	262	5	deg
Number of strides averaged	n/a	131	131	

Table 4.3: Comparison of simulation and physical results for gait 2 of the Active Energy Removal *v1* controller.

Property	Simulation	Robot AVG	Robot STD	Units
Touch-down angle	7.06	7.47	1.26	deg
Lift-off angle	-11.14	-11.40	1.48	deg
Minimum stance height	-6.6	-6.5	0.4	cm
Apex height	11.5	10.9	0.7	cm
Stance time	0.137	0.140	0.001	s
Forward velocity	0.69	0.70	0.05	m/s
Crank actuator angle at lift-off	256	260	3	deg
Number of strides averaged	n/a	154	154	

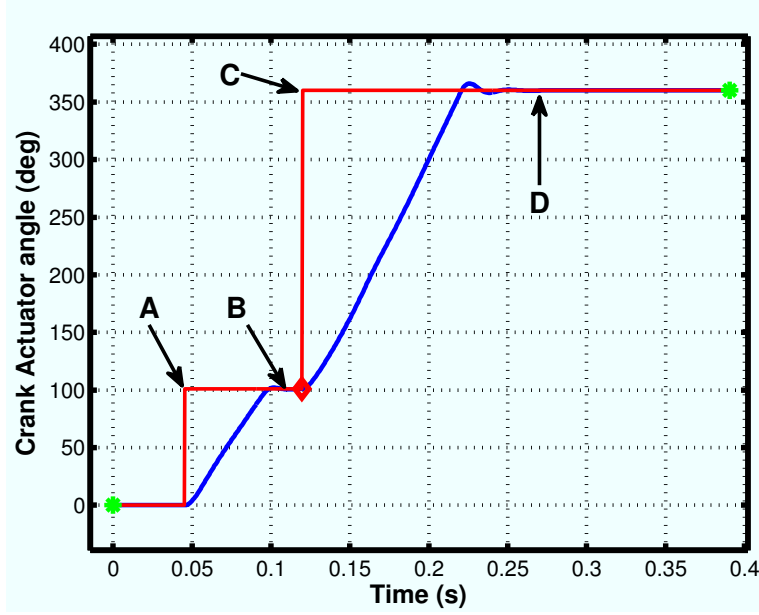


Figure 4.1: Crank actuator angle during the course of one stride for the Fixed Thrust controller. Red line indicates the desired position, while the blue line is the actual position. The green circles represent touch-down events, and the red diamond is lift-off. At 0.046 seconds the assumed maximum compression event occurs (A). A fixed thrust to a crank angle of 100 deg is commanded, and the desired angle is achieved 15 ms before lift-off (B). At lift-off, the crank is commanded to 360 deg (C). After 150 ms the desired angle is reached (D), and the crank is ready for the next touch down.

profile as the simulation.

4.3 Controller Comparison

A comparison of the recovery rates of the AER *v1* and Fixed Thrust controllers following both drop and raised step perturbations is shown in Figs. 4.8 and 4.9. These results show that the Active Energy Removal controller results in faster recovery than the Fixed Thrust controller, as predicted by the simulation.

4.4 Summary of Experimental Results

Section 4.2 showed that the experimental results matched the simulation predictions adequately for both the Active Energy Removal controller and the Fixed Thrust controller. Despite some inconsistencies in apex height, the decay trend seems to match the simulation in both the apex return map and the apex height versus stride

Table 4.4: Comparison of simulation and physical results for gait 3 of the Active Energy Removal *v1* controller.

Property	Simulation	Robot AVG	Robot STD	Units
Touch-down angle	9.74	10.34	1.23	deg
Lift-off angle	-15.26	-15.60	1.45	deg
Minimum stance height	-6.5	-6.7	0.4	cm
Apex height	10.2	10.5	0.7	cm
Stance time	0.132	0.134	0.001	s
Forward velocity	0.98	1.01	0.05	m/s
Crank actuator angle at lift-off	262	254	3	deg
Number of strides averaged	n/a	112	112	

Table 4.5: Comparison of simulation and physical results for gait 1 of the Fixed Thrust controller.

Property	Simulation	Robot AVG	Robot STD	Units
Touch-down angle	3.08	3.74	0.49	deg
Lift-off angle	-5.01	-5.55	0.52	deg
Minimum stance height	-7.1	-7.1	0.4	cm
Apex height	11.2	9.9	0.5	cm
Stance time	0.115	0.122	0.001	s
Forward velocity	0.37	0.39	0.04	m/s
Crank actuator angle at lift-off	179	179	0	deg
Number of strides averaged	n/a	188	188	

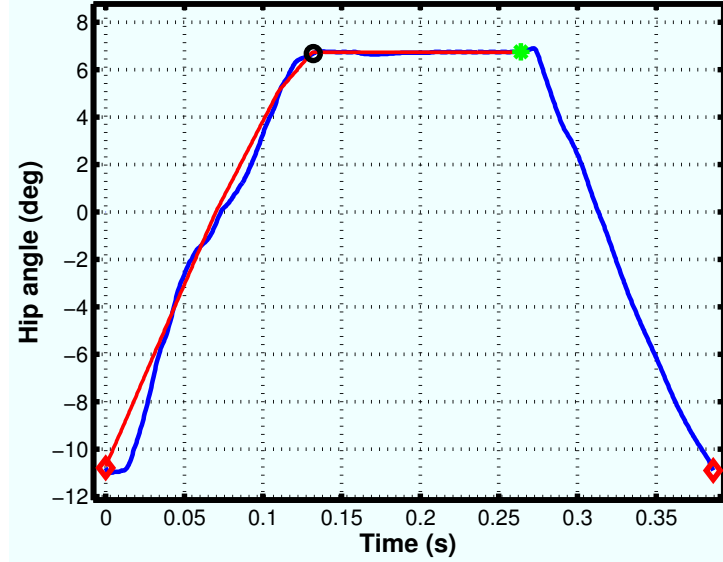


Figure 4.2: Hip actuator angle during the course of one stride for the Fixed Thrust controller. Red line indicates the desired position, while the blue line is the actual position. The green circle represents the touch-down event, the red diamonds are lift-off events, and the black circle is apex. This shows the hip motor is able to position the leg to the correct angle just before apex.

number figures. Stance time was a recurring dissimilarity in all of the tables, with the physical system stance time always being longer than the simulation predicted. This can be explained by foot slip at touch-down by the physical system. When the foot slips, it delays the touch-down as far as the center of mass is concerned, despite triggering a touchdown event in the software via the ground contact switch. This would result in stance times that appear to be longer than expected, but most likely are not longer in reality.

Section 4.3 illustrated that the Active Energy Removal controller stabilizes faster than the Fixed Thrust controller for the gaits tested, when traversing over both drop and raised step perturbations equal to 25% of the nominal leg length. This corresponds to the expectations of the simulation.

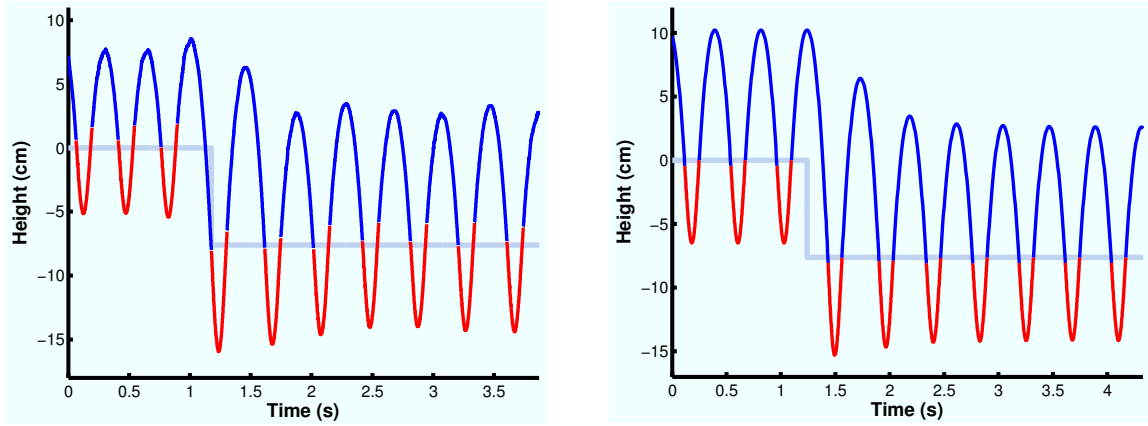


Figure 4.3: COM height of robot (left) and simulation (right) before and after a drop step perturbation for gait 2 of the Active Energy Removal controller. Nominal leg length has been subtracted from COM height for illustration purposes.

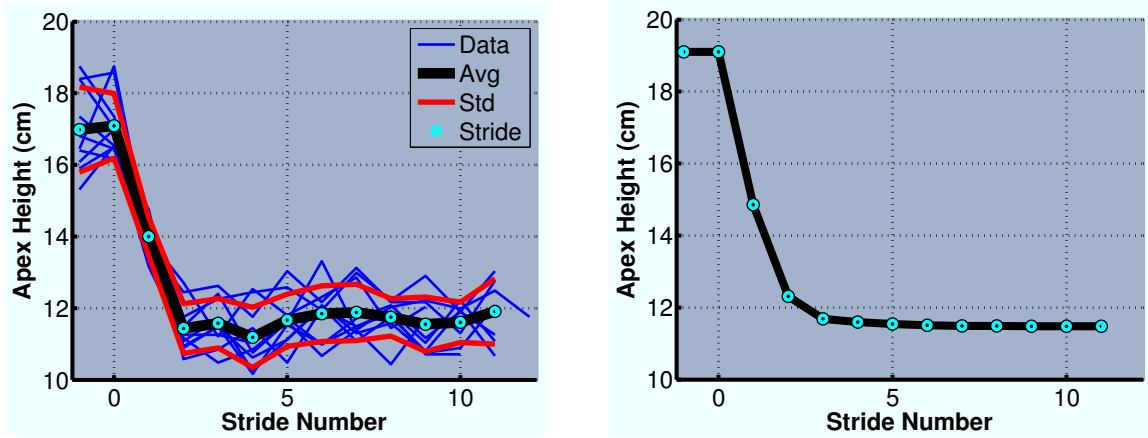


Figure 4.4: Apex height of robot and simulation before and after a drop step perturbation for gait 2 of the Active Energy Removal controller.

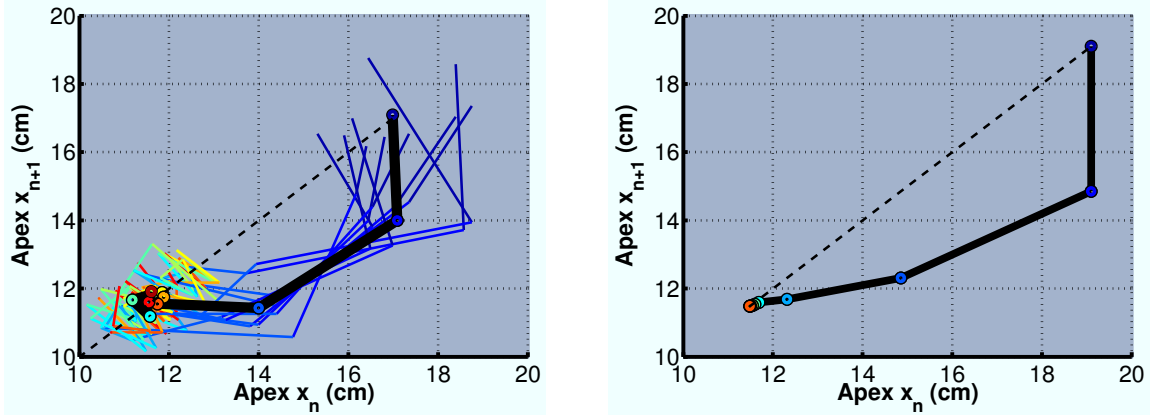


Figure 4.5: Apex return map of robot and simulation before and after a drop step perturbation for gait 2 of the Active Energy Removal controller.

Table 4.6: Comparison of simulation and physical results for gait 2 of the Fixed Thrust controller.

Property	Simulation	Robot AVG	Robot STD	Units
Touch-down angle	6.74	7.54	0.92	deg
Lift-off angle	-10.94	-11.68	0.96	deg
Minimum stance height	-7.2	-7.0	0.5	cm
Apex height	11.4	8.9	0.7	cm
Stance time	0.114	0.123	0.002	s
Forward velocity	0.81	0.82	0.06	m/s
Crank actuator angle at lift-off	191	191	0	deg
Number of strides averaged	n/a	109	109	

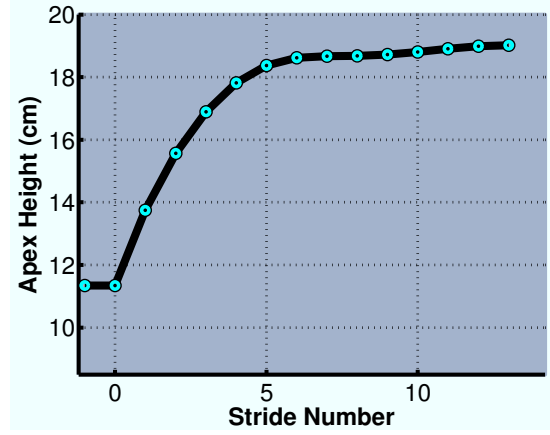
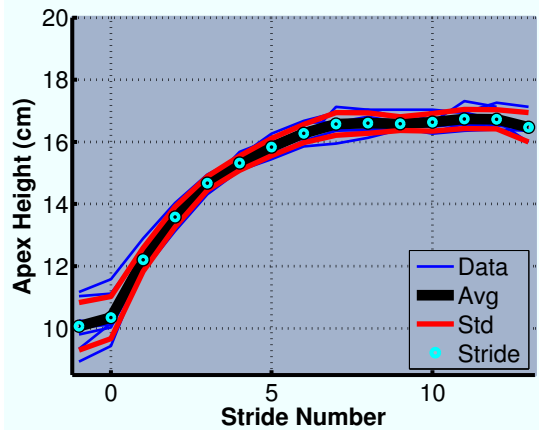


Figure 4.6: Apex height of robot and simulation before and after a raised step perturbation for gait 2 of the Fixed Thrust controller.

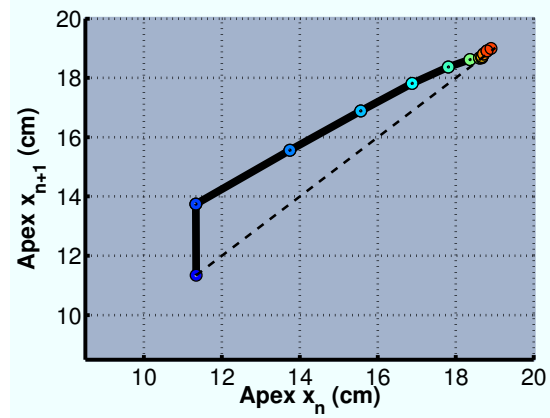
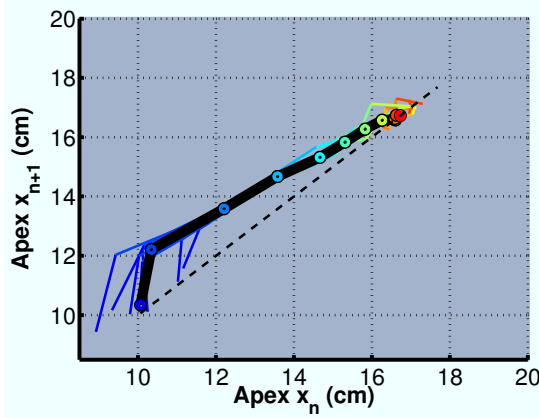


Figure 4.7: Apex return map of robot and simulation before and after a raised step perturbation for gait 2 of the Fixed Thrust controller.

Table 4.7: Comparison of simulation and physical results for gait 3 of the Fixed Thrust controller.

Property	Simulation	Robot AVG	Robot STD	Units
Touch-down angle	10.35	10.21	0.76	deg
Lift-off angle	-17.21	-17.43	0.92	deg
Minimum stance height	-7.2	-6.9	0.3	cm
Apex height	10.4	7.9	0.7	cm
Stance time	0.114	0.125	0.002	s
Forward velocity	1.25	1.15	0.05	m/s
Crank actuator angle at lift-off	219	221	1	deg
Number of strides averaged	n/a	147	147	

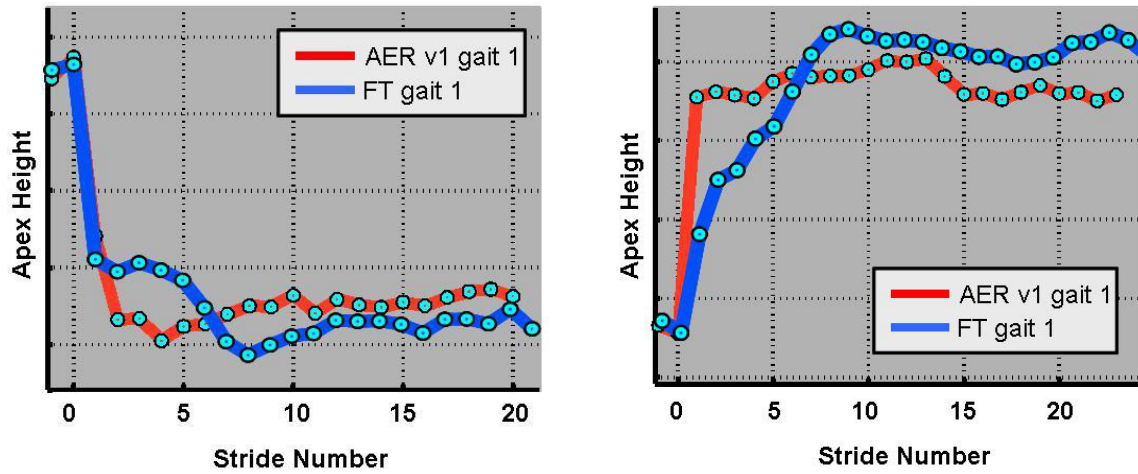


Figure 4.8: Apex height of the Active Energy Removal *v1* and Fixed Thrust controllers following a drop (left) and raised (right) step perturbation. Gait 1.

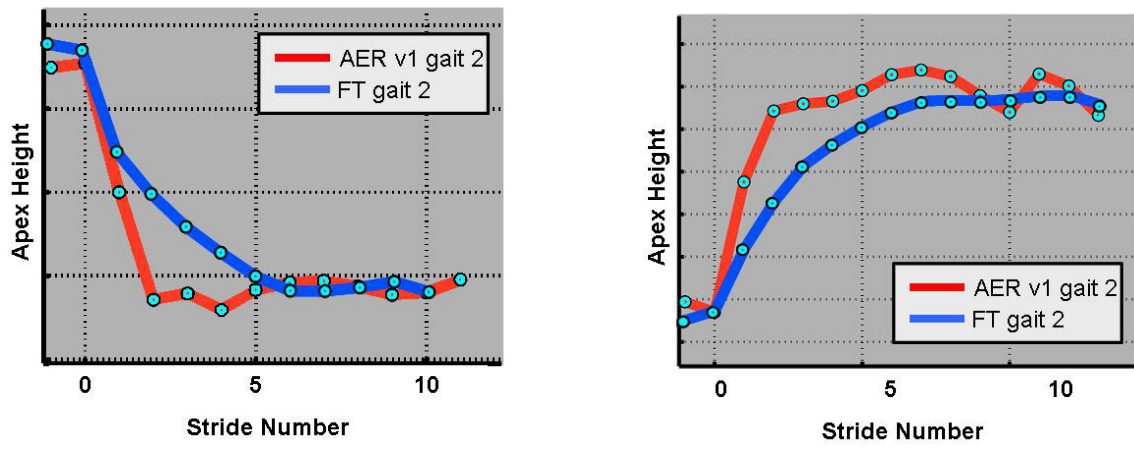


Figure 4.9: Average apex height of the Active Energy Removal *v1* and Fixed Thrust controllers following a drop (left) and raised (right) step perturbation. Gait 2.

CHAPTER 5

CONCLUSIONS

5.1 Conclusions

Simulation results of a lossless system utilizing a novel control scheme that actively removes energy and is capable of traversing unknown, rough terrain were presented by Schmitt. A one-legged SLIP model based hopping robot able to employ the Active Energy Removal controller and withstand both drop and raised step perturbations of at least 25% of the nominal leg length was designed and implemented. Expanding this robotic leg to a four or six legged device to create a rugged autonomous robot capable of handling unknown rough terrain is both feasible and shows promise. An electronic control system was developed as well, to allow for control of the physical system. A non-conservative SLIP model simulation was then designed to match the physical system, and was verified as being accurate by correctly predicting gait characteristics for multiple gaits on two different controllers.

Two versions of the Active Energy Removal controller were simulated and found to be functionally equivalent on this system. Next, simulation results were presented suggesting that the Swing Leg Retraction control law utilizing leg length actuation resulted in gaits that were not as stable as those using the adaptive leg angle control law and the same method of actuation. As a basis of comparison, a classic controller proposed by Raibert was adapted for use on a minimal sensing robot and simulated as well. The simulation results indicated that only the Active Energy Removal controller and the classic controller needed to be implemented on the physical system.

‘Optimal’ gaits found in brute force parameter searching were run on the physical system both on level ground and step perturbations: attesting to the feasibility of the Active Energy Removal controller on a real-world system. The experimental results were used to verify the predictions of the simulation and concluded that, for the ‘optimal’ gaits tested, the Active Energy Removal controller is more stable than the Fixed Thrust controller.

Additionally, a preliminary investigation was made to determine the relationship between system damping, stability, forward velocity, and the amount of energy actively removed. Results from this investigation show that while the most stable gait is a gait with active energy removal, gaits not utilizing active energy removal but with

similar stability (in some cases) exist with almost twice the forward velocity. This suggests active energy removal should only be used when forward velocity is not a concern, but maximum stability is.

5.2 Future Work

There are many directions to go from here. It would be interesting to see a comparison made between the same three controllers from this paper implementing a hip actuation during stance, as opposed to leg length. These three hip actuated controllers could then be compared to the leg length actuation results outlined in this paper.

The individual components of each controller should be examined and compared. For example, a controller utilizing the Fixed Thrust leg angle control law and a controller using the AER leg angle control law should both be implemented with Fixed Thrust energy addition and compared. This would allow for the comparison of the two leg angle control laws with the same actuation.

The possibility of a hybrid controller was mentioned in Sec. 3.4.4: a further look into various combinations of controllers might lead to positive results. For example, a controller that actively removes energy at slower forward velocities and shifts to only adding energy at higher forward velocities could improve gait characteristics.

A stability metric utilizing decay ratio was presented here, and justifications for its use were given. An in-depth comparison of various dynamic stability metrics would be useful to many researchers in legged robotics.

Perhaps the most interesting is determining the optimal total amount of energy removal (both passively and actively) required for fast, stable locomotion. This would allow the controller to adjust the amount of actively removed energy to accommodate to various terrain types and conditions.

Additionally, once the best control approach is found, this system could be duplicated and implemented on a multi-legged autonomous robot.

BIBLIOGRAPHY

- [1] Marc H. Raibert. Legged robots. *Commun. ACM*, 29(6):499–514, 1986. [1.1](#), [1.6.1](#)
- [2] R. Altendorfer, D. Koditschek, and P. Holmes. Stability analysis of a clock-driven rigid-body slip model for rhex. *I. J. Robotic Res.*, 23(10-11):1001–1012, 2004. [1.1](#)
- [3] Uluc Saranli, Martin Buehler, and Daniel E. Koditschek. RHex: A Simple and Highly Mobile Hexapod Robot. *The International Journal of Robotics Research*, 20(7):616–631, 2001. [1.1](#)
- [4] Buehler Battaglia, M. Buehler, R. Battaglia, A. Cocosco, G. Hawker, J. Sarkis, and K. Yamazaki. Scout: A simple quadruped that walks, climbs, and runs. In *IEEE Int. Conf. Robotics and Automation*, pages 1707–1712, 1998. [1.1](#)
- [5] K. Matsuoka. A mechanical model of repetitive hopping movements. *J. Biomech.*, 5:251–258, 1980. [1.2](#)
- [6] M. Raibert and H. Benjamin Brown. Experiments in balance with a 2d one-legged hopping machine. *ASME Journal of Dynamic Systems, Measurement, and Control*, 106:75–81, 1984. [1.2](#), [1.5](#)
- [7] M. Raibert, M. Chepponis, and H. Benjamin Brown. Experiments in balance with a 3d one-legged hopping machine. *International Journal of Robotics Research*, 3:75–92, 1984. [1.2](#)
- [8] P. Gregorio, M. Ahmadi, and M. Buehler. Experiments with an electrically actuated planar hopping robot. *Experimental Robotics*, III:269–281, 1994. [1.2](#)
- [9] M. Ahmadi and M. Buehler. The arl monopod ii running robot: control and energetics. volume 3, pages 1689–1694 vol.3, 1999. [1.2](#)
- [10] R. McN. Alexander and A. Vernon. Mechanics of hopping by kangaroos (macropodidae). *Journal of Zoology*, 303:265–303, 1975. [1.2](#)
- [11] R. Blickhan and R.J. Full. Similarity in multilegged locomotion: Bouncing like a monopod. *Journal of Comparative Physiology*, 173(5):509–517, 1993. [1.2](#)

- [12] R. Full and D. Koditschek. Templates and anchors: Neuromechanical hypotheses of legged locomotion on land. *Journal of Experimental Biology*, 202:3325–3332, 1999. [1.2](#)
- [13] J. Schmitt. Incorporating energy variations into controlled sagittal plane locomotion dynamics. In *proceedings of the ASME International Design, Engineering and Technical Conference*, 2007. [1.3.1](#), [1.5](#), [1.6.3](#), [1.6.3](#)
- [14] R. Full, T. Kubow, J. Schmitt, P. Holmes, and D. Koditschek. Quantifying dynamic stability and maneuverability in legged locomotion. *Integ. and Comp. Biol*, 42:129–157, 2002. [1.4](#)
- [15] Monica A. Daley and Andrew A. Biewener. Running over rough terrain reveals limb control for intrinsic stability. *proceedings of the National Academy of Sciences of the United States of America*, 103(42):15681–15686, Oct 17 2006. [1.4](#)
- [16] J. Cham, S. Bailey, J. Clark, and R. Full. Fast and robust: Hexapedal robots via shape deposition manufacturing. *International Journal of Robotics Research*, 21:869–882, 2002. [1.4](#)
- [17] R. Full, D. Stokes, A. Ahn, and R. Josephson. Energy absorption during running by leg muscles in a cockroach. *Journal of Experimental Biology*, 201:997–1012, 1998. [1.5](#)
- [18] A. Biewener and M. Daley. Unsteady locomotion: integrating muscle function with whole body dynamics and neuromuscular control. *J. Exp. Biol*, 210:2949–2960, 2007. [1.5](#)
- [19] Andre Seyfarth, Hartmut Geyer, and Hugh Herr. Swing-leg retraction: a simple control model for stable running. *J Exp Biol*, 206(15):2547–2555, 2003. [1.5](#), [1.6.2](#)
- [20] J Schmitt and J Clark. Modeling posture-dependent leg actuation in sagittal plane locomotion. *Bioinspiration & Biomimetics*, 4(4):046005, 2009. [1.6.3](#), [3.4.3](#)
- [21] J. Clark, D. Goldman, P. Lin, G. Lynch, T. Chen, H. Komsuoglu, R. Full, and D. Koditschek. Design of a bio-inspired dynamical vertical climbing robot. In *Proceedings of Robotics: Science and Systems*, Atlanta, GA, USA, June 2007. [2.2](#)

BIOGRAPHICAL SKETCH

Benjamin Andrews was born April 15, 1984 in Tallahassee, Florida. He received a Bachelor of Science in Computer Science from Florida State University in 2007 and a Master of Science in Mechanical Engineering from Florida State University in 2010. He is a Boy Scouts of America Eagle Scout and a member of both the Honor Society for the Computing Sciences (UPE) and the Association for Computing Machinery (ACM). He has served as a Research Assistant in the Department of Mechanical Engineering at Florida State University.